BNL-210886-2019-JAAM

JGR Atmospheres

RESEARCH ARTICLE
10.1029/2018JD029471

Key Points:
- SOM analysis is used to define the main synoptic regimes over the Ross Ice Shelf and the WAIS; corresponding cloud properties are examined
- McMurdo clouds are strongly affected by regional forcings that offset the synoptic regime forcing (which dictates the WAIS variability)
- Increasing cyclonic activity near the Antarctic coasts promotes ice-cloud contribution to the radiatively opaque regime

Supporting Information:
- Supporting Information S1

Correspondence to:
I. Silber,
israel0silber@gmail.com

Citation:
Silber, I., Verlinde, J., Cadeddu, M., Flynn, C. J., Vogelmann, A. M., & Eloranta, E. W. (2019). Antarctic cloud macrophysical, thermodynamic phase, and atmospheric inversion coupling properties at McMurdo Station—Part II: Radiative impact during different synoptic regimes. *Journal of Geophysical Research: Atmospheres*, *124*, 1697–1719. https://doi.org/10.1029/2018JD029471

Received 10 AUG 2018
Accepted 14 JAN 2019
Accepted article online 21 JAN 2019
Published online 5 FEB 2019

Antarctic Cloud Macrophysical, Thermodynamic Phase, and Atmospheric Inversion Coupling Properties at McMurdo Station—Part II: Radiative Impact During Different Synoptic Regimes

Israel Silber[1], Johannes Verlinde[1], Maria Cadeddu[2], Connor J. Flynn[3], Andrew M. Vogelmann[4], and Edwin W. Eloranta[5]

[1]Department of Meteorology and Atmospheric Science, Pennsylvania State University, University Park, PA, USA, [2]Argonne National Laboratory, Argonne, IL, USA, [3]Pacific Northwest National Laboratory, Richland, WA, USA, [4]Brookhaven National Laboratory, Upton, NY, USA, [5]Space Science and Engineering Center, University of Wisconsin, Madison, WI, USA

Abstract Different cloud types are generated over Antarctica as a result of various synoptic conditions. The cloud characteristics affect their impact on the surface energy budget. In this study, the dominating synoptic regimes over Antarctica (centered on the Ross Ice Shelf) are classified using self-organizing map analysis, applied over long-term ERA-Interim 700-hPa geopotential height data. The corresponding cloud properties over McMurdo Station (measured as part of the AWARE campaign) are described and discussed with respect to the synoptic settings and sea-ice extent conditions. Cloud radiative forcing calculations are performed as well, and a particular focus is given to the net longwave "radiatively cloudy/opaque" (RO) regime. These results are compared with measurements performed at the West Antarctic Ice Sheet (WAIS) Divide to examine their variability and applicability to other Antarctic locations. It is found that the McMurdo cloud properties are strongly affected by the regional flow patterns and mesoscale cyclonic activity, which often moderates the larger-scale synoptic regime influence. In contrast, the WAIS clouds are more susceptible to the varying synoptic settings. It is suggested that the positive trend in the (frequent) cyclonic activity near the Antarctic coastal regions makes ice clouds an increasingly prominent contributor for the RO cases, especially during freezeup and maximum sea-ice conditions.

1. Introduction

Polar clouds strongly affect the surface energy budget via modifications of the downwelling radiation (e.g., Bennartz et al., 2013; Flournoy et al., 2016; Persson et al., 2002; Sedlar et al., 2012; Shupe & Intrieri, 2004; Stramler et al., 2011; Zuidema et al., 2005). The cloud radiative impact can be significant even in cases of optically thin clouds that are made of liquid droplets (e.g., Bennartz et al., 2013; Turner, Vogelmann, et al., 2007), or when the entire cloud consists of ice hydrometeors (e.g., Flournoy et al., 2016; Miller et al., 2015). Melting events reported in previous studies were linked to the cloud radiative forcing, both in the Arctic (e.g., Bennartz et al., 2013) and Antarctica (e.g., Nicolas et al., 2017).

While a lot of effort has been invested in Arctic cloud research (e.g., de Boer et al., 2009; Shupe et al., 2011, 2013; Sotiropoulou et al., 2016), the harsh conditions and lack of suitable infrastructure have hampered the deployment of extensive field campaigns and the operation of a comprehensive ground-based cloud measurement suite in Antarctica. Therefore, the broad multi-instrument full-year data set from McMurdo Station (77.85°S, 166.72°E; Figure 1) and the summertime measurements acquired at the West Antarctic Ice Sheet (WAIS) Divide (79.47°S, 112.08°W; Figure 1) facilitate a unique opportunity to characterize and study Antarctic clouds. These observations of clouds and the surface radiative budget, gathered as part of the U.S. Department of Energy Atmospheric Radiation Measurement (ARM) Facility's (Mather & Voyles, 2013) 2016 ARM West Antarctic Radiation Experiment (AWARE) field campaign (Lubin et al., 2015; Witze, 2016), are necessary for evaluation of Antarctic cloud processes and their representation in radiative transfer schemes in climate models.

The complex topography surrounding McMurdo Station causes cloud occurrence to vary with the wind direction (Monaghan et al., 2005). The coupling of the cold-air katabatic winds with synoptic activity makes the Ross Ice Shelf (RIS) a highly active cyclogenetic region (Figure 1; Carrasco et al., 2003; Simmonds et al.,

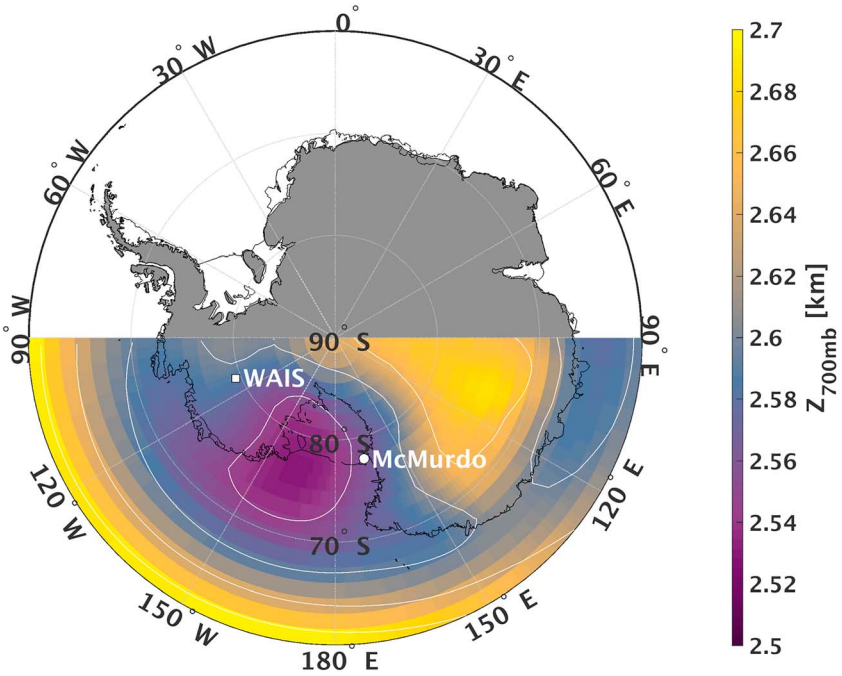

Figure 1. 1979–2017 mean 700-hPa geopotential height (Z) in the Antarctic domain used in this study. The locations of McMurdo Station and the West Antarctic Ice Sheet Divide are marked by the white circle and square, respectively. The low Z over the Ross Ice Shelf provides an indication of that region being highly cyclogenetic.

2003). Mesoscale and synoptic-scale cyclones influence semipermanent flow patterns such as the Ross Air Stream (RAS; Nigro & Cassano, 2014; Seefeldt & Cassano, 2012; Steinhoff et al., 2009) and act as the main source of heat and moisture to the McMurdo region via advection of marine air (Carrasco et al., 2003; Carrasco & Bromwich, 1993; Monaghan et al., 2005; Nicolas & Bromwich, 2011). However, during the period of maximum sea-ice extent in winter, some mesoscale systems do not seem to develop significant cloud signatures due to lack of moisture (Carrasco et al., 2003). Recently, Jolly et al. (2018) examined the phase and vertical distribution of cloud occurrence over the RIS in different synoptic conditions using 4 years of satellite measurements. They concluded that some cloud properties (e.g., cloud water phase) are associated more with the different seasons than synoptic conditions, while others (e.g., clear-sky variability) are influenced more by the synoptic regime.

While the studies mentioned above provided a thorough general description of cloud occurrence and phase over Ross Island during different synoptic regimes, a detailed depiction of the typical cloud properties (e.g., water phase, liquid cloud base height, liquid water content, and radiative forcing) during these regimes is currently missing, although some comprehensive case studies did demonstrate variations in these cloud characteristics during different settings (e.g., Scott & Lubin, 2014). In this paper, self-organizing map (SOM) analysis (Kohonen, 1982, 2013) is used to classify the synoptic modes over half of the Antarctic continent, longitudinally centered over the RIS, using long-term ERA-Interim (Dee et al., 2011) reanalysis data. The hydrometeor characteristics over McMurdo Station measured during the AWARE campaign in 2016 are examined in each of these synoptic regimes, together with the cloud radiative forcing (CRF). Finally, the representativeness of the McMurdo results with respect to the Antarctic ice sheet are evaluated by a comparison with a similar analysis based on the WAIS Divide deployment data.

2. Measurements and Methodology

2.1. SOM Classification

The SOM classification algorithm (a brief general description of this methodology is given in the appendix in Johnson et al., 2008) is applied on four times daily ERA-Interim reanalysis data from 1979 to 2017 (39 years) of the 700-hPa geopotential height anomalies (with a spatial resolution of 1.5° × 1.5°),

covering the latitude and longitude ranges between 90°S to 60°S and 90°E to 90°W, respectively. This 700-hPa data field highlights signatures of pressure systems that predominantly affect the surface. However, although 700 hPa is typically high enough to capture most of the local surface-induced airflow perturbations, large parts of the Antarctic ice sheet and some of the Antarctic mountains (e.g., the Transantarctic Mountain range) are high enough to significantly influence atmospheric parameters at this pressure level (Figure 1; see also Figure 1 in Silber, Verlinde, Eloranta, & Cadeddu, 2018). Therefore, the SOM analysis is performed on anomalies (which also emphasize the geopotential height variations and patterns). The anomalies are calculated by subtracting the 39-year mean map from the data. Each grid point is standardized, that is, divided by its 39-year standard deviation (σ), to prevent the SOM analysis from giving a larger weight to some, highly variable, grid points at the expense of others. Long-term (1979–2017) reanalysis data are used for this classification instead of data spanning only the AWARE campaign (i.e., 2016) to increase the probability of the SOM analysis convergence to a global rather than a local parameter-space minimum. In addition, implementation of long-term data accounts for biases resulting from trends in Antarctic circulation, induced by changes in stratospheric ozone and greenhouse gases concentrations (e.g., Kushner et al., 2001; S. Lee & Feldstein, 2013; Polvani et al., 2010).

The SOM classification applied here utilizes 3 × 3 grid-topology neurons with an initial neighborhood distance of 3 (counting distances by the number of links between neurons). This choice provides nine synoptic modes in total. Previous studies described ways to objectively examine if SOM patterns are distinguishable when the data samples are independent or weakly dependent (e.g., Chang & Johnson, 2015; Johnson, 2013). However, as the consecutive maps used in this study are highly dependent, there is no objective method (to the extent of the authors knowledge) to examine whether the SOM patterns are distinguishable. Nevertheless, it is reasonable to assume that there is no degeneracy in such a small SOM grid size, given the large annual variability of the Antarctic atmosphere.

2.2. McMurdo Station Measurements and Utilized Parameters

The hydrometeor properties from 1 January to 31 December 2016 at McMurdo are derived, following the methodology given in Part I of this series of papers (Silber, Verlinde, Eloranta, & Cadeddu, 2018). In brief, high spectral resolution lidar (HSRL; Eloranta, 2005) data are combined with Ka-Band ARM Zenith Radar (KAZR; Widener et al., 2012) data to generate hourly hydrometeor-bearing air-volume (hereafter referred to as cloud) masks. HSRL cloud returns are classified into ice hydrometeor or liquid-bearing air volumes based on monthly particulate backscatter cross section (β_p) versus linear depolarization ratio (LDR) two-dimensional histograms. KAZR-only cloud returns (based on a signal-to-noise threshold of −16 dB) are classified as clouds of "unknown" phase (see Silber, Verlinde, Eloranta, & Cadeddu, 2018).

Cloud and liquid-bearing cloud layer (LBCL) geometrical properties are obtained from the resolved cloud masks. For the statistics presented in this paper, any cloudy (liquid) grid point must have an hourly cloud (or liquid-bearing) occurrence fraction of at least 25% (15 min). Comparisons with the 10-s resolution AWARE data (see Silber, Verlinde, Eloranta, & Cadeddu, 2018) indicate that this may result in an overestimation of up to 3.5% (~7%) in cloud (LBCL) occurrence fractions on a seasonal basis (not shown).

Additional cloud and surface hourly-mean parameters are used in this study. Ice water path (IWP) values are estimated (for qualitative purposes) by using the KAZR reflectivity and (linearly interpolated) sounding temperature measurements, applying the Hogan et al. (2006) ice water content retrieval method and integrating the results over the cloud profile. Liquid water path (LWP) information (available after 1 February 2016; 88% complete relative to the full data set) is extracted from the two-channel microwave radiometer (MWR; Morris, 2006) measurements (e.g., Fielding et al., 2015; Nicolas et al., 2017; Silber, Verlinde, Eloranta, & Cadeddu, 2018), with a typical uncertainty of ~25 g/m^2 (Cadeddu et al., 2007; Turner, Clough, et al., 2007; Westwater et al., 2001). This parameter is used in combination with the HSRL to determine the total LBCL occurrence fraction (see Silber, Verlinde, Eloranta, & Cadeddu, 2018). A G-Band Vapor Radiometer Profiler (GVRP; Cadeddu, 2010), which produces (in combination with the MWR measurements) a LWP product with an uncertainty as low as ~10 g/m^2 (Cadeddu et al., 2009), was also operated at McMurdo Station from mid-June until the end of the AWARE campaign. The combined MWR-GVRP data product is utilized when possible, but for consistency purposes, the LWP data are treated in this analysis as having the MWR-only retrieval uncertainty. Finally, net longwave (LW) and shortwave (SW) surface radiation

data are calculated by combining the upwelling and downwelling radiation measurements acquired by the ground radiation radiometers (GNDRAD) and the sky radiation radiometers (SKYRAD; Andreas et al., 2018). The total (hemispheric) downwelling SW radiation is represented by the sum of the SKYRAD direct and diffuse downwelling SW component measurements. SW data gathered during periods when the SKYRAD direct downwelling SW component was shaded (by various obstacles; 17% of all the daytime data; see Figure S1 in the supporting information) are removed from the analysis. The CRF is calculated by combining these radiation measurements with results from the Rapid Radiative Transfer Model (RRTM; Mlawer et al., 1997), as explained below in section 2.4.

2.3. WAIS Divide Measurements and Utilized Parameters

The instrument suite for the short WAIS Divide deployment (6 December 2015 to 17 January 2016) was much smaller than at McMurdo Station. Most significantly, it did not include a HSRL or radar; hence, IWP estimates cannot be calculated. However, a micropulse lidar (MPL) with depolarization capabilities (Flynn et al., 2007) was continuously operated throughout the campaign. Using the MPL data (processed by the authors into 30-s and 15-m temporal and vertical resolutions, respectively; Silber et al., 2018c), a water phase-classified cloud mask is generated by estimating the β_p (see Silber et al., 2018b) and classifying the lidar returns in resemblance with the HSRL processing, with a few modifications described in Appendix A. These modifications are required because of the uncertainty in the estimated β_p and the frequent atmospheric temperatures (throughout the campaign) within the plate ice-crystal growth regime that may significantly impact the lidar measurements even at 4° tilting angle (see Appendix A in Silber et al., 2018b). The added processing steps involve the ceilometer cloud base height (CBH) data product (Morris, 2016) and the MPL liquid CBH (LCBH) data product (Silber et al., 2018a). It is important to note that although clouds in the Antarctic interior are predominantly optically thin (e.g., Mahesh et al., 2001), the MPL pulse can still be completely attenuated by occasional optically thick cloud layers (e.g., during the passage of frontal systems). Without radar measurements, the real cloud top, and hence, geometrical integrated thickness, will be underestimated by the MPL in these situations.

In addition to the MPL cloud mask, SKYRAD, GNDRAD, and Surface Energy Balance System (SEBS; Cook, 2018) hourly mean data from the WAIS Divide are utilized for the net radiation and CRF calculations (SEBS upwelling LW data, available from 7 December 2015 are used for the LW calculations due to dubious GNDRAD LW measurements). It should be noted that a comparison between the available hourly SEBS and GNDRAD LW data from McMurdo Station showed excellent correspondence (both instruments measure at equivalent bands; mean upwelling LW difference of 0.2 W/m^2; $R^2 = 0.94$). LWP information extracted from the colocated MWR and GVRP (starting on 19 December 2015 51% complete relative to the full data set) is employed as well, whenever valid data exist.

2.4. CRF Calculations

The RRTM is used in this study to calculate the clear-sky surface net LW and SW radiation for when clouds are present. The configuration of the LW and SW versions of the model is described in Appendix B.

Clear-sky periods (hourly total cloud fraction equal to 0, while assuming no aerosols in the profile) are used to evaluate the deviation of the model output from the measurements. The σ of the model-measurement deviation (for the entire data set) is taken as the model retrieval uncertainty, and the clear-sky mean offset (model minus observations) is added to the measured fluxes during the cloudy periods. The removal of data from periods when the direct downwelling SW component was shaded reduced the SW uncertainty by nearly 25% (see Table S1). The σ at McMurdo and the WAIS are larger in the SW (15.0 and 7.3 W/m^2, respectively) than in the LW (5.9 and 6.1 W/m^2, respectively). The SW offset magnitude of 6.3 W/m^2 (0.4 W/m^2) is higher (lower) than the LW offset of 1.6 W/m^2 (4.9 W/m^2) at McMurdo (WAIS). The median SW and LW offset magnitude percentages at both sites (relative to the measured net radiation absolute values) are lower than 8%. The relatively higher SW uncertainty at both sites can be the result of lack of aerosols in the model and/or very thin high-level undetected clouds in the assimilated atmospheric profiles. The influence of ozone variability on the downwelling SW radiation (via the Chappuis bands; see Brion et al., 1998) was thoroughly examined for potential improvement of the SW uncertainties. However, a consideration of this factor was eventually omitted from this analysis, as it did not show a significant reduction in the uncertainty (see Figure S2).

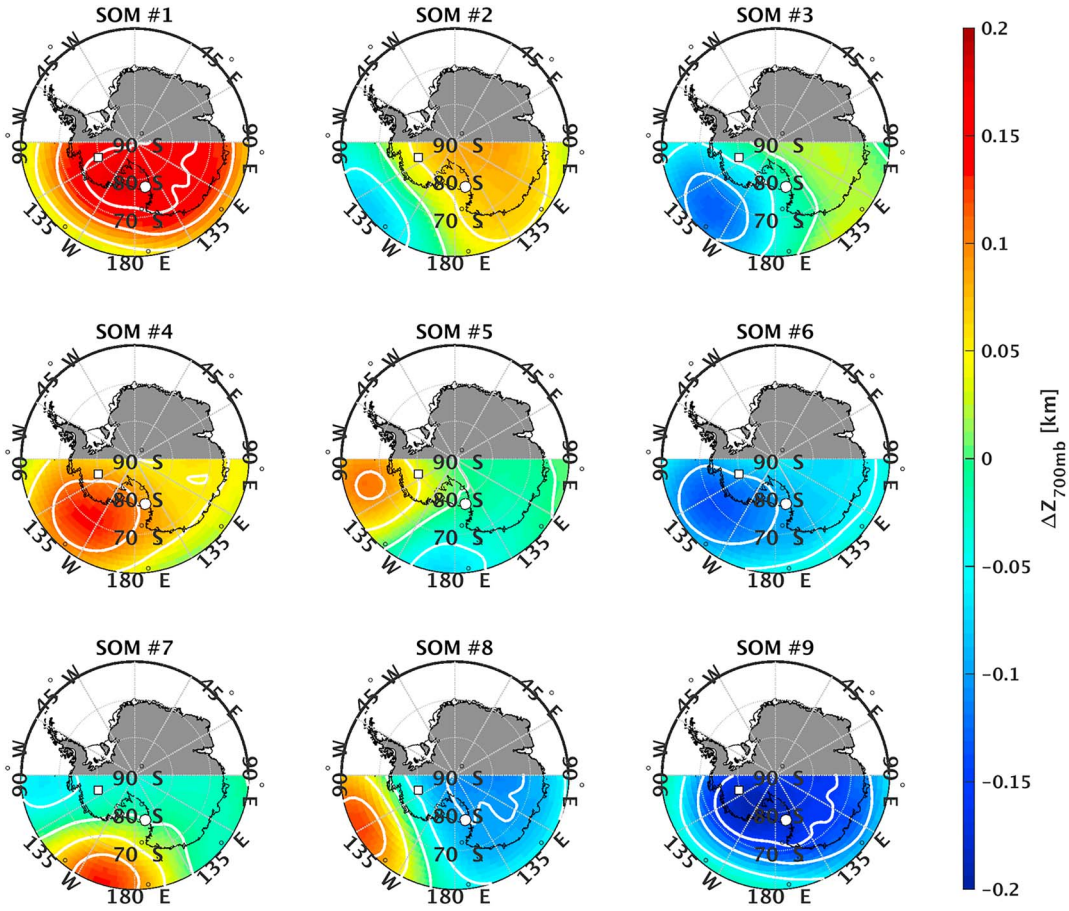

Figure 2. Self-organizing map (SOM) analysis results showing the dominating 700-hPa *Z* anomaly patterns. The white contours designate the *Z* anomalies with a spacing of 0.05 km. The locations of McMurdo Station and the West Antarctic Ice Sheet Divide are marked by the white circle and square, respectively.

The LW CRF (CRF_{LW}) is calculated by

$$CRF_{LW} = (LW_{obs}\downarrow - LW_{obs}\uparrow) - (LW_{clr}\downarrow - LW_{clr}\uparrow), \quad (1)$$

where the arrows indicate the upwelling and downwelling radiation, and *obs* and *clr* denote the observed fluxes and the corresponding modeled clear-sky fluxes, respectively (a similar methodology was used by Miller et al., 2015). The CRF_{LW} is the total CRF (CRF_{tot}) during nighttime periods. For daytime periods, CRF_{tot} is calculated by

$$CRF_{tot} = (LW_{obs}\downarrow - LW_{obs}\uparrow + SW_{obs}\downarrow - SW_{obs}\uparrow) - (LW_{clr}\downarrow - LW_{clr}\uparrow + SW_{clr}\downarrow - SW_{clr}\uparrow). \quad (2)$$

3. Results

3.1. Synoptic Regimes

Figure 2 shows the dominating 700-hPa synoptic pattern prototypes (hereafter, simply referred to as SOMs) as determined by the SOM analysis. SOM analysis is considered to be a consistent method, which is less prone to errors relative to other classification methods (e.g., *K*-means clustering; see Bação et al., 2005). Nonetheless, the SOM analysis was repeated 10 times to test the robustness of these results (as the SOM algorithm is computationally expensive, a higher number of repetitions was not used; e.g., Johnson, 2013). These runs showed the same general patterns, with a minimum grid point Pearson's correlation coefficient of 0.998 (using all the map grid points), while considering rotation of the SOM analysis grid (which is possible

Table 1
SOM Analysis Summary, Including the Typical Main Season of Occurrence Determined Based on Sea-Ice Extent

SOM #	Description	Main season of occurrence
1	High over the entire Antarctic continent (negative SAM index)	MELT, MNSI
2	Low centered to the north of the Amundsen Sea (with tendency toward a negative SAM index)	MELT, MNSI
3	Low centered in the Amundsen Sea	All (tendency to FRZ)
4	High over the Ross and Amundsen Seas (with tendency toward a negative SAM index)	MELT, MNSI
5	High between the Amundsen and Bellingshausen Seas; low to the west	All (tendency to FRZ)
6	Low over the Ross Ice Shelf, West Antarctica, and the Ross and Amundsen Seas (with tendency toward a positive SAM index)	FRZ, MXSI
7	High centered to the north of the Ross Sea; low over the Bellingshausen Sea	All (tendency to MNSI)
8	High centered to the north of the Amundsen Sea (with tendency toward a positive SAM index)	FRZ, MXSI
9	Low over the entire Antarctic continent (positive SAM index)	MXSI

Note. SOM = self-organizing map; SAM = Southern Annular Mode; MNSI = minimum sea-ice extent; FRZ = freezeup; MXSI = maximum sea-ice; MELT = melt. See text for details.

because of a symmetric grid utilization; see Kohonen, 1982). SOM analysis tests performed using smaller domains surrounding Ross Island resulted in essentially the same SOMs (not shown).

The different SOMs show various configurations of low- and high-pressure systems surrounding Antarctica, which are described in Table 1. SOMs 2, 3, 6, and 7 represent several modes of the Amundsen-Bellinghousen Seas Low (ABSL; Coggins & McDonald, 2015; Fogt et al., 2012; Hosking et al., 2013), while SOMs 1 and 9 designate the distinct negative and positive phases of the Southern Annular Mode (SAM; Hartmann & Lo, 1998; Limpasuvan & Hartmann, 1999), respectively. As part of the grid topology configuration of the SOM analysis nodes, the neighboring nodes, that is, SOMs 2 and 4 (6 and 8) for SOM 1 (9), have a tendency for the same SAM condition, while SOMs 3, 5, and 7 are characterized by a "neutral" SAM state.

The utilization of long-term data in the SOM analysis enables the examination of trends. Figure 3 depicts the evolution of the annual relative occurrence of each SOM. The dotted-blue lines mark the apparent long-term trend of each SOM (calculated using a least squares linear fit; trend slope is given in the title of each panel).

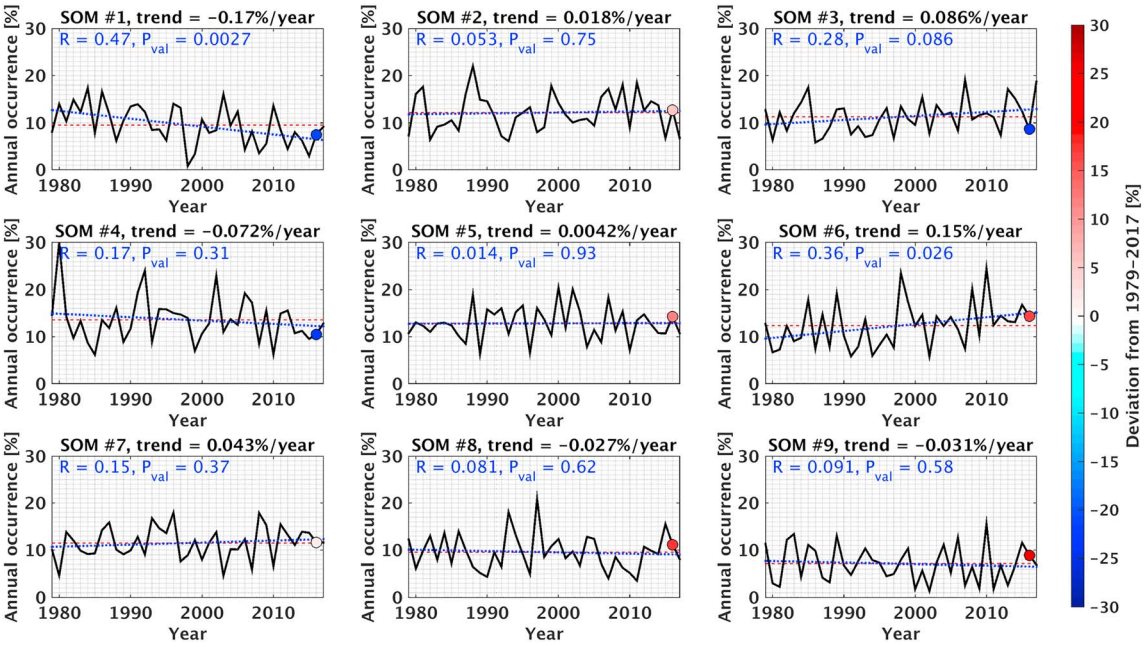

Figure 3. Annual self-organizing map (SOM) pattern occurrence between 1979 and 2017. The dashed red lines indicate the long-term annual means of occurrence. The colored circles denote the 2016 value and its deviation from the long-term mean. The dotted blue lines illustrate the (least squares fitted) long-term trends. Trend slopes are given in the title of each panel, and the Pearson's correlation coefficient (R) for the trend line and the data are shown in each panel, together with its calculated P value.

Out of the nine SOMs, only two)SOMs 1 and 6) show statistically significant long-term trends (correlation coefficient and p value for each linear fit are shown in each panel), from which SOM 1 exhibits the greatest slope. The decreasing trend in this SOM is attributed to the long-term increase in the positive SAM index driven by stratospheric ozone decline and greenhouse gas forcing (Lee & Feldstein, 2013) that is most pronounced around summer months (Marshall et al., 2004; S. Solomon et al., 2007, section 3.6.5). The long-term incline in the occurrence of SOM 6 (which represents a relatively deeper westward ABSL) is associated with the long-term increase in the cyclonic activity over the RIS and its surroundings (see Figure 9 in Simmonds et al., 2003) and potentially also the multidecadal deepening of the ABSL (Raphael et al., 2016), both of which may be linked to the positive SAM index trend as well (e.g., Fogt et al., 2012; Hosking et al., 2013; Sinclair et al., 1997; Uotila et al., 2013).

The annual mean relative occurrence of each SOM is denoted by the dashed red line in each panel of Figure 3. Examination of the 2016 relative occurrence deviation from that 39-year mean (indicated by the color of the circle markers) shows that the AWARE campaign can reasonably represent the long-term patterns on an annual basis, with deviations that do not exceed 30% (see also Figure 4a).

The high sensitivity of Antarctic cloudiness to the sea-ice extent (Bromwich et al., 2012) stresses the need to partition the data into seasons based on this parameter (measured by satellited instruments; see Cavalieri et al., 1996; Maslanik & Stroeve, 1999): minimum sea-ice extent (MNSI; defined here as a total Antarctic sea-ice extent area $<5{\cdot}10^6$ km^2; equivalent to summer), maximum sea-ice extent (MXSI; defined here as a total Antarctic sea-ice extent area $\geq 15{\cdot}10^6$ km^2; equivalent to winter), freezeup (FRZ; equivalent to autumn), and melt (MELT; equivalent to spring). For example, in 2016, the MNSI, FRZ, MXSI, and MELT seasons began on 14 January, 24 March, 5 July, and 11 November, respectively. These starting dates are within the long-term (1979–2017) sea-ice variability interquartile range, except for MELT, which started 10 days earlier than the lower interquartile range limit.

Figures 4c–4f portray the mean annual occurrence of each SOM in different seasons, together with the occurrence σ. Some of the SOMs (e.g., SOMs 1, 4, and 9) are predominantely observed in specific seasons, while others (e.g., SOM 5) occur fairly uniformly in all seasons (see also Table 1). Unlike the annual comparison, the 2016 SOM seasonal occurrence occasionally deviate from the long-term mean by several hundred percents; for example, in the MNSI season SOM 1 did not occur at all during 2016, while the long-term relative occurrence is almost 15%. Conversely, SOM 6 occurred nearly eight times more than the long-term average in that season. The climatological SOM occurrence differences between the MELT and MNSI seasons are either small or have an opposite sign relative to these anomalous 2016 MNSI occurrences (Figures 4c and 4f). Therefore, the MNSI deviations from the long-term mean in SOMs 1, 3, 4, 6, and 9 cannot be explained by the early MNSI beginning in 2016 (relative to the sea-ice extent climatology).

Similar to the MNSI season, the FRZ and MELT seasons show large (though smaller) deviations from the long-term means. The 2016 SOM occurrence during the MXSI season did not significantly deviate from the long-term mean (~60% at the most, and consistently within the mean $\pm\ \sigma$). Thus, full-season cloud statistics from AWARE (cloud properties weighted by the 2016 SOM occurrence) represent the long-term pattern mainly during the MXSI season. Nonetheless, cloud characteristics are analyzed separately (regardless of their occurrence) for each SOM and as a function of season. Therefore, the results presented here can be representative and used as an outlook of the long-term behavior if every year is separately weighted based on the SOM seasonal occurrence, while assuming that the cloud properties measured in 2016 represent their SOM climatological characteristics.

3.2. Cloud Properties at McMurdo Station

Figure 5 depicts the main cloud properties in different SOMs and seasons. Statistics where the 2016 seasonal mean relative occurrence fractions (Figures 4c–4f) fall below 4% are displayed in transparent colors and omitted from this discussion, because the small sample sizes are not representative of the climatology. The bars in the left panels of Figure 5 designate the total cloud occurrence fractions (bar height). The color division of each bar represents the distribution of the cloud integrated thickness (total depth of all hydrometeor-bearing air volumes in the profile), while the circle and rectangle markers denote the mean and median cloud integrated thickness, respectively. The box-and-whisker plot in each panel describes

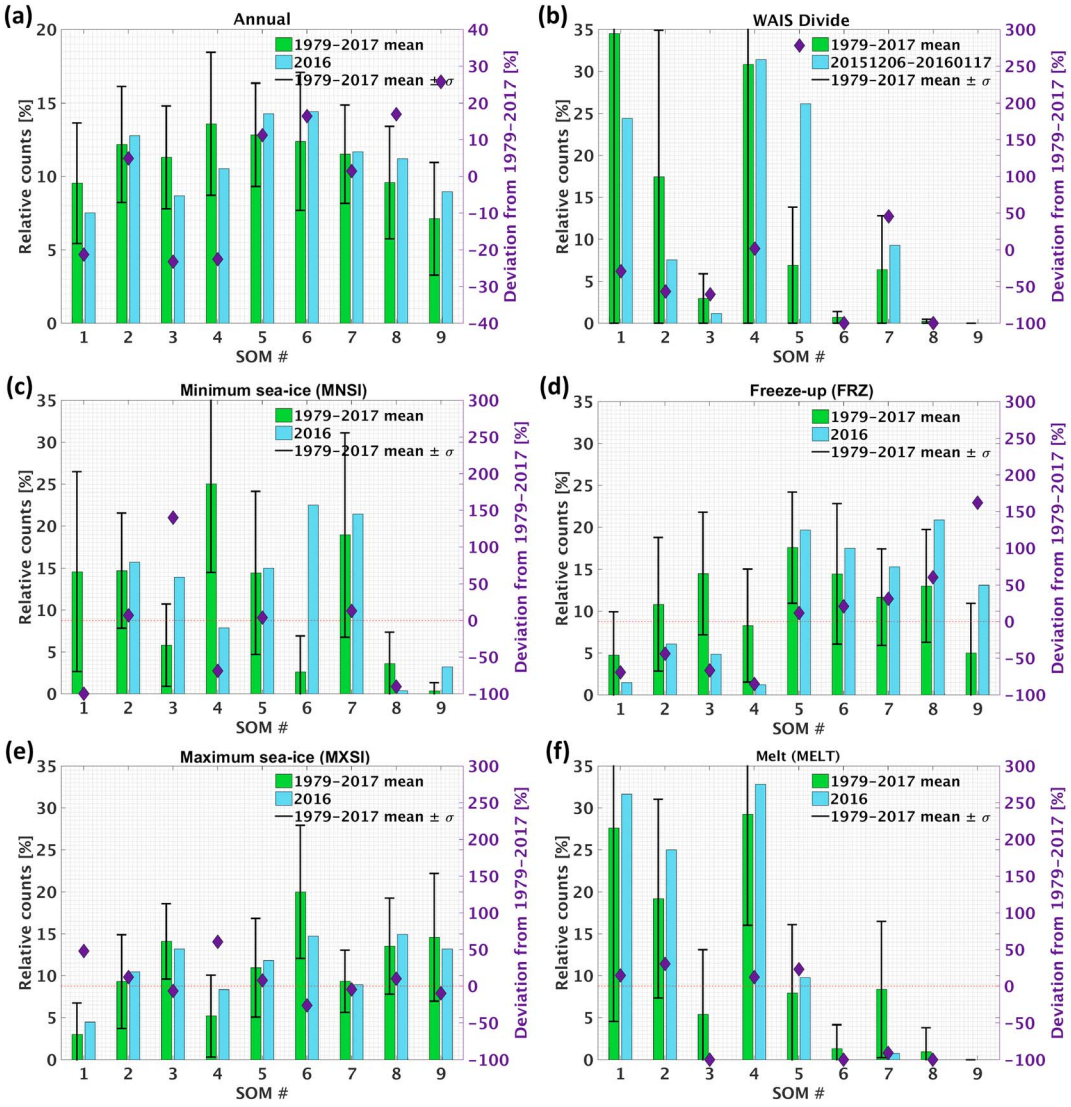

Figure 4. (a) 1979–2017 mean annual occurrence of each self-organizing map (SOM) pattern together with the 2016 (McMurdo deployment) occurrence percentage. The error bars represent the mean occurrence ± the standard deviation (σ), while the purple markers denote the deviation of the 2016 values from the long-term means. (b) Same, but for the period merely covering the West Antarctic Ice Sheet (WAIS) Divide deployment. (c–f) Same, but for seasons determined by minimum sea-ice extent (MNSI), freezeup (FRZ), maximum sea-ice extent (MXSI), and MELT (MELT), respectively. The "minimum" ("maximum") sea-ice extent season is defined by sea-ice extent below (equal or above) 5 (15) million square kilometers.

the estimated log-scaled IWP. The right panels in Figure 5 are similar to the left panels but with the bars and markers representing the LBCL occurrence fraction and LWP statistics, and the box-and-whisker plots describing the lowest detected LCBH. The black section of each bar designates profiles where the HSRL detects a LBCL, while the MWR retrievals show LWP values below the instrument's uncertainty level of ~25 g/m^2, a value in which liquid clouds almost become radiatively opaque in the LW regime (see Figure SB1 in Turner, Vogelmann, et al., 2007). The gray-colored sections designate periods with a HSRL-detected LBCL in the profile during which the MWR retrieval calculations did not converge or no MWR data exist. As the MWR was not operating at McMurdo during January, most of the gray sections occurred during the MNSI and MELT seasons.

MNSI season clouds have somewhat similar characteristics in all of the SOMs (Figures 5a and 5b); their total occurrence fractions exceed 64%, with thicknesses typically less than 4 km with moderate to large amounts of ice. Liquid water is detected 38–60% of the time (more than 57% given cloud occurrence in each SOM). The highest cloud occurrence fractions (>90%) are in SOMs 2 and 6. SOM 6 exhibits a median cloud thickness of

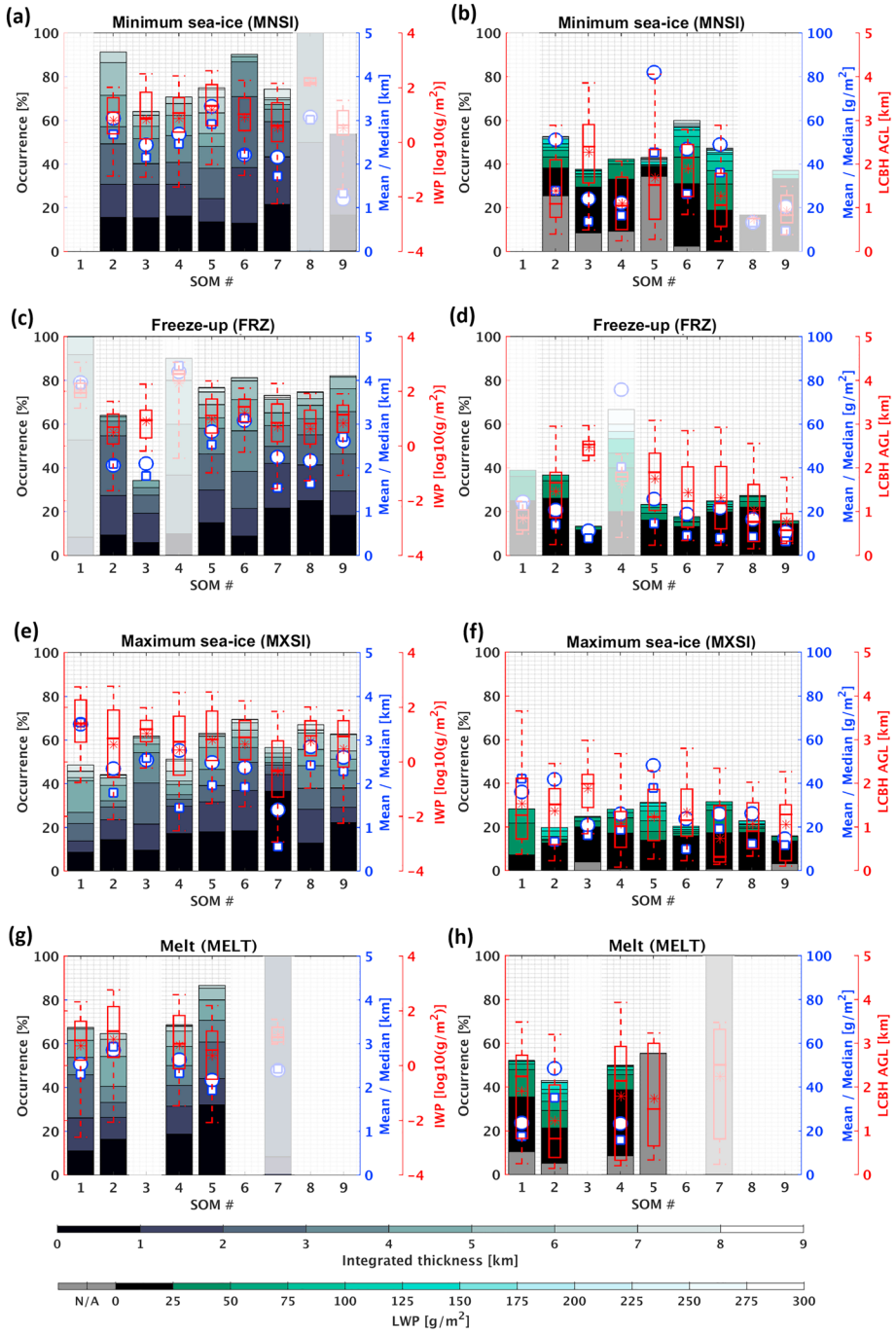

Figure 5. (Left panels) Total cloud occurrence fraction at McMurdo Station (bar height) and integrated thickness (bar color division) during the nine synoptic regimes. Results from different seasons are shown in rows. The circle and rectangle markers represent the mean and median cloud integrated thickness, respectively. The box-and-whisker plots denote the median (thick line), 1st and 3rd quartiles (box's edges), 5th and 95th percentiles (whisker's edges), and mean (asterisk) of the estimated log-scaled ice water path (IWP) during each synoptic pattern in each season. Statistics where the 2016 seasonal mean relative occurrence fractions (Figures 4c–4f) fall below 4% are displayed in faint colors. (Right panels) Same, but with the bars and markers representing the liquid-bearing cloud layer (LBCL) occurrence fraction and liquid water path (LWP) statistics, and the box-and-whisker plots describing the lowest detected liquid cloud base height (LCBH) above ground level (AGL). The black color in the bars designates periods when the high spectral resolution lidar (HSRL) detected a liquid layer, while the two-channel microwave radiometer (MWR) retrievals show LWP values below the instrument's uncertainty level of ~25 g/m^2. Similarly, the gray color symbolizes periods with a liquid layer detected in the profile by the HSRL, during which the MWR retrieval calculations did not converge, or no MWR data exist.

~2.2 km (and a total thickness between 1 and 3 km in 58% of the SOM occurrence). These SOM 6 clouds are often (~67%) accompanied by liquid water. However, the LWP in these liquid layer occurrences is rather low (median and mean of ~26 and 47 g/m^2, respectively), probably due to the typical protracted flow across the WAIS and the RIS. SOM 2, in which the low is to the north of the Amundsen Sea, shows thicker clouds (higher median value by ~450 m) and slightly larger amounts of liquid (median and mean LWP values of ~28 and 51 g/m^2, respectively), largely concentrated at lower levels (median lowest LCBH of ~1.1 km, more than 1 km below SOM 6). These differences might be related to the ABSL configuration relative to McMurdo (see Coggins & McDonald, 2015), and the common advection of heat and moisture to the Antarctic coasts during the negative phase of the SAM (Sen Gupta & England, 2006). The thickest clouds (thicker than 7 km in more than 4% of the time this SOM occurs) are seen in SOM 5, when the low is to the north of McMurdo. The LBCLs in these SOM 5 clouds are found at various levels (note the large LCBH spread between the 5th and 95th percentiles).

The differences between the SOMs become more pronounced in the FRZ season. With the exception of SOM 3, cloud occurrence fractions are still high (above 64%), but LBCLs are relatively rare and their LWP is low (Figures 5c and 5d). The low cloud occurrence fractions in SOM 3 could be attributed in part to a generally southerly katabatic flow of dry and cold air toward McMurdo from the inner continent. Although the hourly based analysis in this study prevents the direct examination of wave-induced clouds, the consistently high LCBHs and the low LWP (below the MWR uncertainty level) suggest that the LBCLs observed in SOM 3 (with a total occurrence fraction of only ~13%) are most likely generated by orographic lifting induced by airflow over the local topography, for example, Black and White Islands, Minna Bluff, and so forth (Monaghan et al., 2005; Scott & Lubin, 2016).

SOMs 7 to 9 are characterized by westerly airflow anomalies at 700 hPa across the East Antarctic ice sheet to the west of the RIS and Ross Sea. The resulting intensified katabatic flow from East Antarctica onto the RIS, mainly through Terra Nova Bay and Byrd Glacier, often spawn mesoscale cyclones (Bromwich, 1991; Carrasco & Bromwich, 1993). The typical small scale (~200 km; see Carrasco et al., 2003) and short lifetime of these cyclones and their occurrence in various synoptic conditions (Carrasco & Bromwich, 1993) prevent their representation in the SOMs (e.g., Coggins et al., 2014; Seefeldt & Cassano, 2012). Yet the deep clouds with high IWP and the presence of some LBCLs despite the general katabatic flows in SOMs 7 to 9 are indicative of the activity of mesoscale cyclones.

In the MXSI season (Figures **5**e and **5**f) SOMs 1, 4, 5, and 7 show considerable percentages of LBCL presence and occurrence given cloud, exceeding 28% and 44% in each case, respectively. The MXSI conditions imply that considerable amounts of moisture are drawn onto the RIS by generally northerly flow, likely in part by "atmospheric rivers" (e.g., Gorodetskaya et al., 2014). In SOM 7 conditions, water vapor is predominantly advected at the low levels (the lowest LCBHs are primarily detected below 500 m above ground level [AGL]). These MXSI SOM 7 cases, with LBCL occurrence of ~56% relative to the total cloud manifestation, are largely stratiform low-level mixed-phase clouds: note the relatively low IWP amounts and the integrated thickness <1 km in nearly 65% of the total cloud occurrence. In contrast, the LBCLs are often associated with deep mesoscale cyclogenesis over the RIS region during SOMs 1 and 4. This cyclogenesis may be augmented by warm marine air transport, induced by the high-pressure circulation centered above the Ross and Amundsen Seas (e.g., Carrasco & Bromwich, 1993).

Deep clouds with moderate to large amounts of ice indicate frequent frontal activity in SOM 8 as well, but with significantly lower LBCL occurrence (observed in only ~1/3 of the cloudy periods). The lower LBCL occurrence fraction may be influenced by the weakening of the northerly flow component relative to SOM 7, and the enhanced katabatic flow from East Antarctica that is associated with SOM 8. SOM 6, which is associated with a characteristic katabatic flow from the WAIS onto the RIS, exhibits depleted LBCL frontal activity, similar to SOM 8.

Only four SOMs (1, 2, 4, and 5) were effectively present during the 2016 MELT season (see Figure 4f). The total cloud occurrence fraction in the MELT season is high (Figure 5g), ranging from ~65% in SOM 2 to ~87% in SOM 5. Large ice amounts (comparable to the other seasons) suggest that frontal activity is common in this season as well. However, mean cloud geometrical thicknesses are smaller, and the LBCL occurrence fractions are higher than in the other seasons (LBCL occurrence fraction of at least ~43% in each SOM; Figure 5h).

SOM 5 exhibits the highest LBCL occurrence fraction of ~55% during the MELT season. The high LCBHs in this SOM make the 700-hPa prototype (Figure 2) more representative with regard to the LBCLs; hence, the direct flow from the open ocean in these retreating sea-ice conditions onto the RIS may explain this high occurrence percentage. Unfortunately, all the SOM 5 patterns occurred during January 2016 when no MWR measurements were available, preventing any analysis of LWP characteristics. LWP in SOMs 1, 2, and 4 are relatively high compared to the other seasons, with the highest values observed in SOM 2 (median and mean values of 35 and 48 g/m^2, respectively). This might seem surprising, as the SOM prototype flow suggests dry continental airflow onto the RIS. The typically low LCBH (mostly under 1 km), which could be related to steering of the RAS (e.g., Nigro & Cassano, 2014), may explain the discrepancy between the 700-hPa flow and the higher LWP occurrence. The 700-hPa height used in the SOM analysis may not be representative of the systems that produce the bulk of the moisture advection. Examination of seasonal long-term mean total column water composites of ERA-Interim data during different SOMs supports this argument (not shown). Moreover, the moisture advection patterns are dependent on preceding atmospheric conditions (e.g., the existence of an atmospheric river), which are challenging to characterize in a bulk analysis such as the one presented here. These two important aspects emphasize some of the main weaknesses of the SOM analysis. Persistence of LBCLs is not examined in the SOM context for the same reasons (in addition to the inconsistent and variable SOMs throughout the LBCL life span).

3.3. Statistics of the CRF and the "Radiatively-Opaque" Regime at McMurdo Station

The occurrence frequency of the surface net LW flux for the entire year of 2016 at McMurdo Station is depicted in Figure 6a. Similar to Arctic measurements (e.g., Cesana et al., 2012; Morrison et al., 2012; Pithan et al., 2014; Stramler et al., 2011), two modes (separated at a net LW value of −30 W/m^2) are clearly apparent, namely, the "radiatively clear" (RC), primarily characterized by clear-sky, optically-thin, or high-level clouds, and the "radiatively cloudy" (also referred to as "radiatively opaque" [RO]) state, in which typically low-level optically thick clouds are observed (Stramler et al., 2011). The nodes of these two modes are shifted toward lower net LW values by more than 20 W/m^2 relative to Arctic reports (e.g., Morrison et al., 2012; Stramler et al., 2011). The RC node shift may be attributed to the significantly lower temperatures and drier atmosphere over McMurdo Station (and Antarctica in general) relative to the Arctic region (e.g., Bromwich et al., 2012; Jones et al., 1999). The shift in the RO regime might be associated with the typically higher cloud base over McMurdo relative to the Arctic (e.g., Shupe, 2011; Silber, Verlinde, Eloranta, & Cadeddu, 2018), which principally implies larger temperature differences between the surface and the cloud effective temperature. This shift may also be affected by more tenuous (with lower emissivity) cloud layers, resulting from the drier atmosphere (see Figure 5, right panels; see also Bromwich et al., 2012; Klein et al., 2009; Shupe et al., 2006; Shupe & Intrieri, 2004; Turner, 2005; Turner, Vogelmann, et al., 2007).

While most of the scientific attention with regard to the RO state in polar region studies is given to mixed-phase and liquid clouds (e.g., Cesana et al., 2012; Morrison et al., 2012), it is known that ice-only clouds may generally produce comparable instantaneous LW forcing (e.g., Figures 8 and 10 in Miller et al., 2015). Therefore, the CRF of ice-only cloud profiles is examined here, in addition to the LBCL CRF. Figures 6c–6f illustrate the mean CRF_{LW} in different SOMs and seasons for three types of clouds: clouds containing LBCLs with LWP $\geq$ 25 g/m^2, which typically have near-unity emissivity (Shupe & Intrieri, 2004; Turner, Vogelmann, et al., 2007); clouds containing tenuous LBCLs with LWP $<$ 25 g/m^2 (MWR uncertainty), which have been shown in the past to be capable of exerting significant radiative forcing as well (e.g., Bennartz et al., 2013; Turner, 2007); and ice-only clouds (determined when the combined HSRL and MWR hourly total liquid occurrence fraction is lower than 25%). The red markers designate the percentage of each cloud type profile occurrence when the net LW is within the RO state.

The mean CRF_{LW} of the opaque LBCLs (those with LWP $\geq$ 25 g/m^2) varies between 56 and 75 W/m^2, in any SOM or season. Therefore, the high percentage of these cases in the RO state (100% during FRZ season and close to that during MXSI conditions) is expected. The CRF_{LW} value consistency is in agreement with the results from Summit, Greenland, reported by Miller et al. (2015). The higher CRF_{LW} values for the same LWP range in the Summit study might be related to the lower cloud base AGL measured at Summit in comparison with McMurdo Station (e.g., Shupe et al., 2013; Silber, Verlinde, Eloranta, & Cadeddu, 2018).

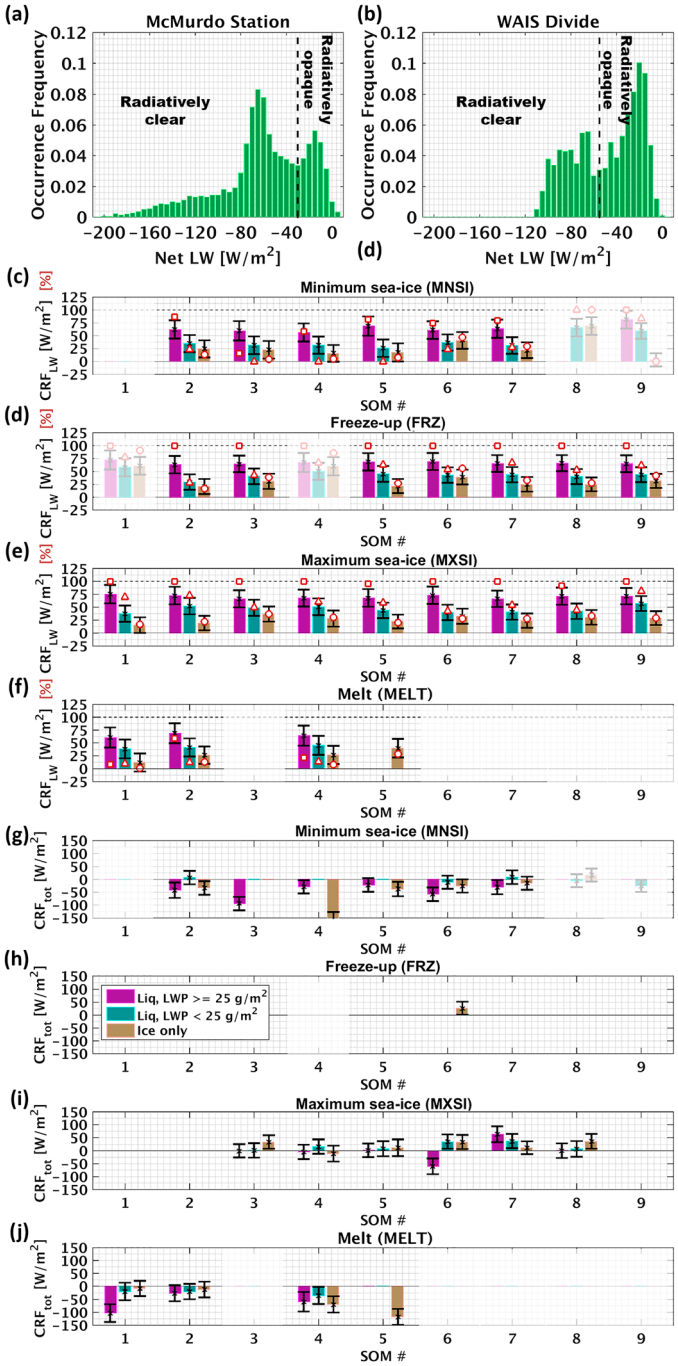

Figure 6. (a) Net longwave (LW) radiation occurrence frequency (bin size of 5 W/m^2) measured at McMurdo Station. The dashed black line separates between the radiatively clear and the radiatively cloudy/opaque (RO) states. (b) Same, but for the West Antarctic Ice Sheet Divide deployment. (c–f) Mean LW cloud radiative forcing (CRF) in different synoptic regimes and seasons of profiles containing liquid-bearing layers with liquid water path (LWP) ≥ 25 g/m^2, profiles with LWP < 25 g/m^2 where liquid-bearing cloud layers (LBCLs) are detected by the HSRL, and profiles where only ice hydrometeors are detected by the high spectral resolution lidar (LBCL hourly occurrence fraction <25%), while the LWP is consistently below 25 g/m^2 (see legend in panel h for details). The error bars represent the combined instrument and Rapid Radiative Transfer Model uncertainties. The red markers (rectangles, LBCLs with LWP ≥ 25 g/m^2; triangles, LBCLs with LWP < 25 g/m^2; circles, ice only) denote the percentage of the cloud type profile occurrence when the net LW is within the RO regime during the specific self-organizing map (SOM) and season (e.g., 100% of the LBCL profiles with LWP ≥ 25 g/m^2 occurring in SOM 1 during the MXSI season have a measured net LW within the RO regime). (g–j) Similar to panels (c–f), but for the total (LW + shortwave) CRF calculated for cases within the RO state during daytime only periods (solar zenith angle <90°).

Tenuous LBCLs tend to have the lowest CRF_{LW} during the MNSI period, fluctuating between 26 and 37 W/m^2. This CRF_{LW} minimum can potentially be linked to the relatively higher LCBHs in this season (see Figure 5b), the height of which (with being tenuous) may also explain some of the low RO percentages (0% in SOMs 3, 4, and 5). The mean ice-only cloud CRF_{LW} is the highest in SOM 6 relative to the other SOMs during MNSI and FRZ (with ~41 and ~39 W/m^2, respectively), but only the second highest in the MXSI season with ~33 W/m^2 (there are no data for SOM 6 during MELT). The frequent synoptic-scale deep frontal activity associated with SOM 6 (and the resulting high IWP) may account for some of this relatively higher CRF_{LW}, probably together with a lower hydrometeor cloud base (often in the form of precipitation).

FRZ and MXSI seasons show similarly tenuous LBCL CRF_{LW} ranging between 30 and 57 W/m^2, with more than 50% of these cases (in total) producing RO patterns. Ice-only clouds exert a lower CRF_{LW} during these seasons typically ranging between 15 and 39 W/m^2, where the high ~37 W/m^2 in SOM 3 during the MXSI season coincides with the high IWP (Figure 5e) and low-level precipitation.

During MELT the tenuous LBCL CRF_{LW} is within their typical range of the FRZ and MXSI seasons, but the percentage of cases in the RO regime is below 14%. The source for this lower RO percentage is larger surface-cloud temperature differences during MELT relative to the other two seasons (not shown). The higher LCBHs during MELT (Figure 5h) and the similar LCBH temperature range within the three seasons (see Figure 8 in Silber, Verlinde, Eloranta, & Cadeddu, 2018) are consistent with these observations.

Ice-only cloud CRF_{LW} in SOM 1 is barely evident during MELT, with a value of ~12 W/m^2 (smaller than the CRF_{LW} error of ~18 W/m^2). Conversely, ice clouds in SOM 5 tend to show high CRF_{LW} of nearly 40 W/m^2, which is likely driven by common frontal activity (as discussed above). The geometrically thinner clouds and the lower IWP relative to the other SOMs in this season suggest that the ice clouds in SOM 5 have lower "effective" cloud bases.

Figure 7 focuses on the RO cases and shows the partitioning of profiles in that state based on the cloud water phase and LWP (total LBCL profiles + ice-only profiles = occurrence of 100%), together with the cloud mean lowest LCBH, integrated thickness, and IWP. With the exception of SOM 3, the MNSI season RO state is dominated by opaque LBCLs. Based on their prevalent low mean LCBH (<1 km), thickness (<2 km) and IWP, it is deduced that these opaque LBCLs are mainly low-level mixed-phase clouds (excluding SOM 5).

The RO state is not common during MNSI in SOM 3 (see Figure 6c), where the southerly katabatic flow onto the RIS originates from cold and dry continental air. When RO clouds do occur in SOM 3, the opaque LBCLs account for 50% of the RO profiles, with the remaining profiles consisting of very thick (>5 km) high IWP ice clouds. Ice clouds continue to dominate the RO state in SOM 3 during FRZ and MXSI (despite the low ice-only percentages seen in Figures 6d and 6e), with clouds containing large ice amounts and typical thicknesses >3 km. These are likely frontal clouds generated in the region of cyclogenesis near Byrd Glacier. High FRZ and MXSI ice-only cloud RO percentages are also seen in SOM 9 and the frontal-dominated SOM 6, both of which are typified by intense katabatic flow (from East Antarctica and the WAIS onto the RIS, respectively). These two SOMs exhibit RO cloud patterns that are similar to those of SOM 3, that is, frontal clouds. In addition, in both of these SOMs, ice-only clouds dominate the RO state during the FRZ and MXSI seasons.

Apart from SOMs 3, 6, and 9, LBCLs (opaque and tenuous) RO cases outnumber the ice-only cases from FRZ to MELT. However, ice-only clouds still account for at least 15% of the RO cases in every SOM and exceed 40% of the total RO cases in SOMs 5, 7, and 8 during FRZ, SOM 8 during the MXSI season, and SOM 4 in MELT. These ice-only cases are generally characterized by thicknesses larger than 3 km (very often above 4 km) with large IWP, suggesting that these clouds RO are associated with frontal activity.

Tenuous LBCL RO occurrence surpasses the opaque LBCL occurrence in all FRZ SOMs (except SOM 2), as well as in SOMs 2, 3, 6, 8, and 9 during the MXSI season, and in SOM 1 during MELT, owing in part to the higher total occurrence of tenuous LBCLs relative to opaque LBCLs (note the black bar sections versus the greenish bar sections in Figures 5d, 5f, and 5h). In nearly half of the SOM-season RO case combinations from FRZ to MELT (SOMs 2, 7, 8, and 9 during FRZ and SOMs 5–9 during MXSI), the clouds containing these tenuous LBCLs predominantly have low thicknesses (below 2 km), low IWP, and LCBHs below 1.5 km. Thus, it is inferred that the low LCBHs cause these (lower emissivity) clouds to render LW downwelling radiation comparable to the surface upwelling radiation.

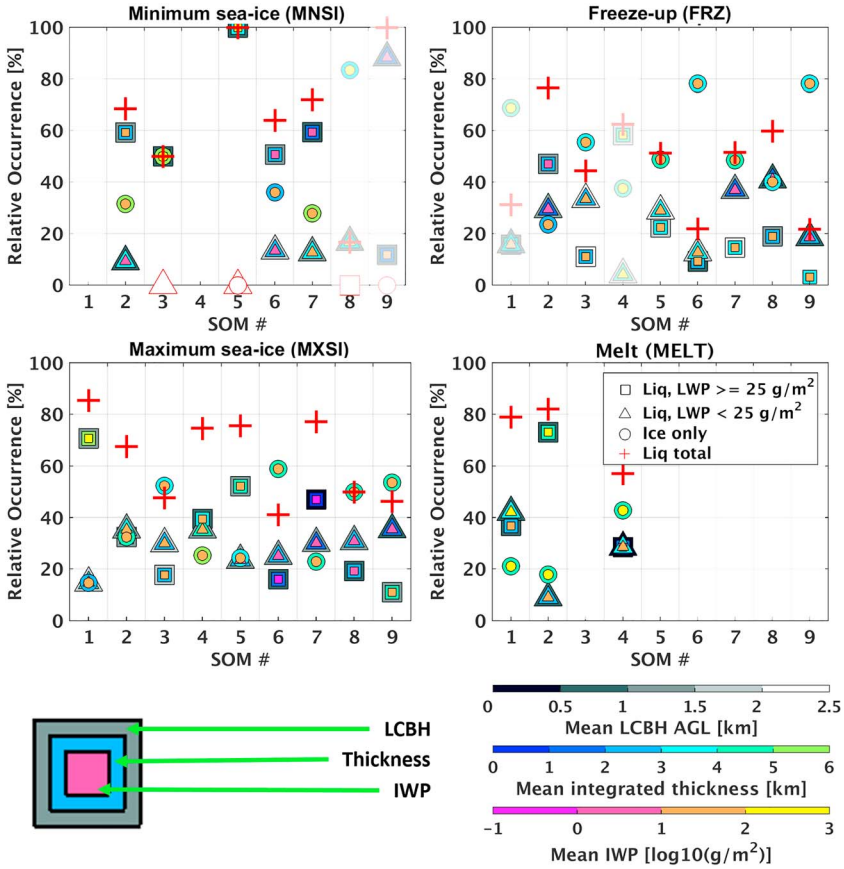

Figure 7. Mean lowest liquid cloud base height (LCBH), integrated thickness, and ice water path (IWP) within the radiatively cloudy/opaque (RO) regime (net LW ≥ −30 W/m^2 at McMurdo Station) in different seasons and governing synoptic patterns. The *y*-axis values (height) of the rectangle, triangle, and circle markers represent the occurrence of profiles containing liquid-bearing cloud layers (LBCLs) with liquid water path (LWP) ≥ 25 g/m^2, profiles with LWP < 25 g/m^2 where LBCLs are detected by the high spectral resolution lidar (HSRL), and profiles where only ice hydrometeors are detected and the LWP is consistently below 25 g/m^2, respectively (occurrence relative to the total amount of RO profiles, where both microwave radiometer and HSRL data are available). The marker colors denote the mean LCBH above ground level (AGL; available only for LBCLs, when detected by the HSRL), mean integrated thickness, and mean IWP, following the color bars and diagram at the bottom of the figure. The "+" marker indicates the total liquid profile (rectangle + triangle) relative occurrence, that is, the total liquid profile occurrence + ice-only occurrence = 100%. The data used to generate this figure are provided in Table S5. SOM = self-organizing map.

Other SOM-season combinations are excluded from this tenuous LBCL characterization. In some of them (e.g., SOM 3 in FRZ and MXSI), the LW imprints of the often wave-induced high-base LBCLs (above 1.5 km) are very likely augmented by the moderate ice amounts (frequently precipitation). In others (e.g., SOM 4 during the MXSI season), the LBCLs are embedded in deep frontal activity (note the high integrated thicknesses).

Similar to the tenuous LBCLs, the opaque LBCLs observed in the RO state are often accompanied by moderate ice amounts (likely precipitation). Alternatively, they can also be part of deep frontal clouds, for example, cyclonic activity in SOM 9 during the MXSI season and SOM 2 during MELT. Similarly, high thicknesses and IWP in SOM 5 during MNSI and MXSI suggest that these opaque LBCLs are associated with mesoscale frontal systems, generated by direct marine air advection from the Ross Sea (see the SOM prototype in Figure 2 and Carrasco & Bromwich, 1993). However, in similarity to most of the opaque LBCLs in the MNSI season, the RO state opaque LBCLs mostly embody low-level mixed phase clouds, for example, SOMs 6–8 during the MXSI season, SOMs 1 and 4 during MELT, and SOM 7 during MXSI.

Figures 6c–6f show that essentially all cloud types produce a positive surface CRF_{LW}, which is equal to the CRF_{tot} in nighttime conditions. However, in daytime conditions the CRF_{tot} (LW + SW) can change its sign.

To emphasize these differences, the CRF_{tot} for daytime conditions is shown in Figure 6g–6j only for the RO state cases. During the MNSI period when the volcanic soil at McMurdo Station is exposed, the SW albedo estimated using equation (A2) is very low (on the order of 0.1–0.2; see Figure S3). These low albedos may result in a substantial SW cloud cooling effect, depending on the overlying cloud transmittance and the solar zenith angle (e.g., Shupe & Intrieri, 2004). For example, the ice-only cloud CRF_{tot} of nearly -159 W/m^2 during SOM 4 (Figure 6g) is mainly based on cloud measurements between 27 and 28 December 2016. The optically thick frontal clouds observed over McMurdo on these dates predominantly consisted of ice hydrometeors (intermittent LBCLs with LWP < 15 g/m^2 were detected less than 4 min per hour on average). The combination of the low surface albedo during the event (~0.1) and the nearly minimal (for McMurdo's coordinates) solar zenith angle resulted in a strong SW cloud cooling effect, which overshadowed the CRF_{LW}.

Figure 6g shows that only the tenuous LBCLs can potentially be emissive enough in the LW to induce strong downwelling radiation, while having a sufficiently high SW transmittance to allow the incoming SW solar radiation to reach the surface. Thus, tenuous LBCLs (relatively common over McMurdo Station; see Figure 5b) are tentatively the main surface heating source (by clouds) during daytime ice-free surface conditions.

In contrast, the SW CRF (CRF_{SW}) over the snow-covered surface (with a high albedo) during the FRZ and MXSI seasons is occasionally sufficiently small compared to the CRF_{LW} and/or close to 0 W/m^2 (from below), so that a distinctly positive CRF_{tot} may be observed for all cloud types (Figures 6h and 6i). Because persistent dry katabatic (Foehn) winds over the McMurdo region often erode the snow cover (Monaghan et al., 2005), the cloud SW cooling effect may become large enough to enable negative CRF_{tot} with high magnitudes during seasons other than summer. Such conditions are observed mainly during the transition seasons (e.g., Figure 6j), but also in SOM 6 in the MXSI season (Figure 6i). SOM 6 was primarily preceded by either SOMs 8 or 9 in 2016, both of which are characterized by intensification of the dry katabatic winds from East Antarctica (see Figure 2).

3.4. WAIS Divide Results

The WAIS Divide campaign results are limited by the smaller instrument suite and the shorter (44 days) summertime deployment. Yet these measurements may provide some valuable insights about the cloud properties above the ice sheet, as well as the representativeness (to some extent) of the McMurdo Station observations.

From a sea-ice extent standpoint, the deployment took place mainly during the MELT season (~91%), with a minor fraction (9%) covering part of the MNSI season. Throughout this period essentially, only 5 SOMs were observed, namely, SOMs 1, 2, 4, 5, and 7 (see Figure 4b). These relative SOM occurrences resemble those during the MELT season in the McMurdo data (Figure 4f).

Figures 8a and 8b portray the LBCL and total cloud statistics, respectively. Lack of a radar and an objective method to determine the MPL pulse extinction altitude inhibits an accurate cloud thickness characterization and direct comparison with the McMurdo results. However, given the low fraction of opaque LBCLs (see Figure 8a) and based on manual examination of the MPL cloud masks, rough estimates can be made with regard to cloud thickness variability, especially when cloud thickness bins less than 1–1.5 km are considered.

SOM 7 appears to be persistently cloudy (total occurrence fraction of ~99%) and exhibits the deepest clouds observed over the WAIS, with more than 32% of the clouds having a thickness of at least 2 km. The clouds in this SOM contain LBCLs at varying heights ~58% of the time. SOM 2 conditions show the lowest cloud (68%) and LBCL (<35%, or ~51% given cloud) occurrence fractions. Unfortunately, the low availability of MWR data precludes LWP information for this SOM (and SOM 1 as well, for which LBCLs are detected 2/3 of the time). Moisture supply to the WAIS Divide is by orographic lifting from the north-northeast and the northwest-west, the latter of which was found to be more efficient in advecting both heat and moisture onto the WAIS (Nicolas & Bromwich, 2011). The archetypal flow in both SOMs 7 and 2 is epitomized by easterly dry continental airflow, which may instigate dry conditions over the WAIS Divide (e.g., SOM 7 patterns as described in Nicolas & Bromwich, 2011). However, small changes in the location of the ABSL in these SOMs can steer moisture onto the WAIS from the northeast (e.g., SOM 7 conditions as shown in Figure 17b in Scott & Lubin, 2014; see also Hosking et al., 2013).

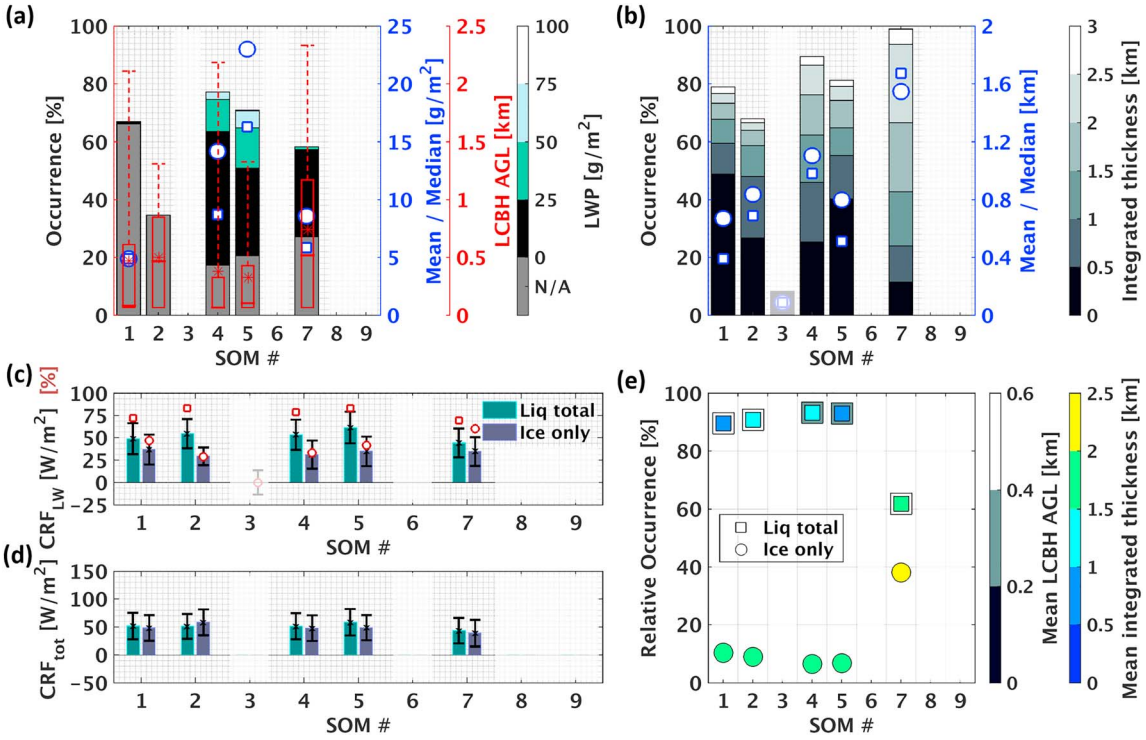

Figure 8. Cloud and radiative properties at the West Antarctic Ice Sheet (WAIS) Divide for the full deployment (~91% melt, 9% minimum sea-ice). (a) Liquid water path (LWP) and lowest liquid cloud base height (LCBH) above ground level (AGL) statistics as in Figure 5. (b) Similar, but for the integrated cloud thickness (as in Figure 5; no ice water path (IWP) data, as there were no radar measurements in this deployment). (c, d) Mean longwave (LW) and total cloud radiative forcing (CRF; in the latter for cases within to the radiatively cloudy/opaque [RO] state) in different synoptic regimes, respectively (similar to Figure 6; the entire deployment took place during daytime, so that all the RO data are used for the total CRF). (e) Mean LCBH and integrated thickness within the RO regime (net LW ≥ -55 W/m^2 at the WAIS Divide) in different synoptic patterns (similar to Figure 7). No LWP-based separation is made in panels (c) to (e) for the liquid-bearing cloud layer (LBCL) profiles due to the low microwave radiometer data availability (~51%). SOM = self-organizing map.

In agreement with the conclusions of Nicolas and Bromwich (2011), SOMs 4 and 5, which are characterized by a northwesterly-westerly flow of warm marine air onto the WAIS (Figure 2), show the highest LBCL occurrence fractions (77% and 71%, respectively). These LBCLs are observed mainly at low levels (note the low LCBHs in Figure 8a). Consequently, intense downwelling LW radiation induced by these cloud layers is often expected at the WAIS in these SOMs. Indeed, these two flow regimes dominated the extensive surface melting event during January 2016 reported by Nicolas et al. (2017).

Comparison of the WAIS cloud properties to those observed over McMurdo Station during MELT shows that the total cloud occurrence fractions are higher and the lowest LCBHs are lower over the WAIS Divide. In addition, the comparison suggests that cloud variability in any specific SOM is lower over the WAIS (e.g., higher cloud thickness bin percentages for a single SOM in the bars depicted in Figure 8b relative to those shown in Figure 5g), while the variability between different SOMs is larger. An example for these variability disparities can be seen in the difference between the minimum and maximum LBCL occurrence fraction; over the WAIS this difference is 43%, while over McMurdo the values are 16% (the high uncertainty with regard to SOM 7 at McMurdo may strongly impact comparison of the total cloud occurrence fraction). Thus, it is deduced that mesoscale cyclogenesis over McMurdo, stemmed from the synoptic regime wind field interaction with the regional topography (e.g., Carrasco et al., 2003; Nigro & Cassano, 2014), as well as other regional flow patterns such as the RAS, may spawn cloud patterns that overshadow the larger-scale synoptically generated cloud fields. This process results in large variations in the cloud properties in specific SOMs, and smaller variations between different SOMs.

The surface net LW flux occurrence frequency for the WAIS deployment is shown in Figure 6b. The RO modal peak location is the same as in the McMurdo data. However, the occurrence frequency values in that regime are significantly higher, due to the higher total cloud and LBCL occurrence fractions, as well as the

lower LCBHs (and despite the low LWP values over the WAIS). The trough separating the RO and RC states is not as distinct as in the McMurdo data and is shifted by ~25 W/m^2 (to −55 W/m^2). The RC regime exhibits multiple peaks. The ambiguity in the node identification might be the result of an insufficient number of observations. The lack of net LW observations below −115 W/m^2 at the WAIS is indicative of the low surface temperatures on clear-sky days, resulting in less (more) upwelling (net) LW radiation.

The CRF_{LW} for the WAIS observations is illustrated in Figure 8c. LBCLs are not separated into tenuous and opaque layers in this and the following panels due to the low MWR data availability. The mean LBCL CRF_{LW} ranges between 44 and 61 W/m^2, lower than the opaque but higher than most of the tenuous LBCL CRF_{LW} during MELT at McMurdo. The lower LWP (based on the available MWR data) suggests that these moderate values are mainly driven by tenuous LBCLs with low LCBHs.

At least 70% of the LBCL profiles in each SOM produce downwelling LW radiation strong enough (relative to the surface upwelling LW radiation) to be associated with the RO state. In all SOMs less than 60% of the ice-only profiles are within that regime.

Figure 8e shows the LBCL and ice-only profile representation in the RO regime, together with their mean lowest LCBH and total integrated thickness. LBCLs dominate the RO state, similar to the MELT observations from McMurdo Station. However, their relative percentages are higher, with more than 89% in SOMs 1, 2, 4, and 5. The low mean LCBH and integrated thickness of these LBCL cases suggest that the RO state over the WAIS Divide is governed (at least during MELT) by low-level mixed-phased clouds. SOM 7 shows that copious ice-only clouds (typically, with thicknesses above 2 km) can render numerous RO cases (more than 38% of the observed RO cases in that SOM). However, the relatively low climatological occurrence of SOM 7 (see Figure 4b) implies that ice-only clouds have little effect on the LW RO state over the WAIS during MELT.

Nonetheless, positive ice-only cloud CRF_{SW} in these infrequent daytime RO cases results in CRF_{tot} (Figure 8d) that is equivalent to the CRF_{tot} of LBCLs in the same SOMs. LBCLs over the WAIS Divide generate smaller CRF_{SW} magnitudes than the ice-only clouds, the signs of which can be negative or positive (SW enhancement; e.g., Nicolas et al., 2017). The ice-covered surface at the WAIS Divide produces significantly different RO LBCL and ice-only CRF_{SW} compared to McMurdo Station during ice-free periods, which do occur in all seasons.

4. Summary and Conclusions

The synoptic patterns affecting the RIS and West Antarctica are diverse and unique. Each of these patterns may affect the flow fields and the resolved cloud properties differently. In this study, dominating patterns were classified using SOM analysis, and the corresponding cloud properties observed over McMurdo Station and the WAIS Divide were analyzed. This type of SOM-based cloud characterization has some limitations. For example, the utilization of data that comprise a single field at a single pressure level may improperly represent and explain the observations in some cases (e.g., moisture advection or cloud condensation at other pressure levels in a decoupled event). In addition, various scenarios (e.g., the formation of an atmospheric river) depend heavily on preceding atmospheric conditions (in multiple-day timescales), which are difficult to characterize in bulk analysis of present synoptic conditions. This also inhibits the study of longer-term phenomena such as persistent mixed-phase clouds, which demand in-depth case studies.

Yet the analysis presented here provides valuable cloud statistics, from which it is concluded that

1. Frequent frontal activity over McMurdo Station makes ice clouds a significant factor in the net surface LW budget, accounting for several tens of percents of the "radiatively opaque" regime events, especially during the FRZ and MXSI seasons.
2. The net surface LW "radiatively opaque" regime over the WAIS is dominated by frequent low-level mixed-phase clouds, at least during MELT. The total CRF of all clouds in this regime is positive during both daytime and nighttime conditions (in agreement with Scott et al., 2017), with equivalent ice-cloud and LBCL daytime magnitudes.
3. Opaque LBCLs generate the highest CRF_{tot} during nighttime conditions, both at McMurdo and the WAIS. However, over McMurdo Station, predominantly tenuous LBCLs may be optically thin enough in the SW and optically thick enough in the LW to induce a positive CRF_{tot} in (ice-free) daytime

conditions. Other cloud types (opaque LBCLs and thick ice clouds) often cool the surface in these conditions, by reflecting more incoming SW radiation than the re-emitted downwelling LW radiation. During MXSI nighttime and ice-covered daytime periods, the CRF over McMurdo Station is very likely similar to other ice-covered Antarctic regions with similar cloud patterns (e.g., LCBH and LWP) and temperature profiles. The MXSI ice cloud CRF agreement with CRF calculations from the South Pole (Town et al., 2005) provides some support for this conclusion.

4. Cloud patterns stemmed from mesoscale frontal activity and regional semipermanent flow patterns around McMurdo Station often dominate the synoptic scale patterns (although mesoscale cyclogenesis depends largely on the synoptic flow regime).
5. This mesoscale forcing domination results in larger variability in the same synoptic patterns (because of the sensitivity to the regional flow fields), and smaller variability between different synoptic patterns, during a specific season. Some patterns, however, still display distinctive characteristics (e.g., SOM 3, characterized by dry airflow and orographic clouds).
6. The clouds over the WAIS Divide show large variability between different synoptic regimes and are more self-consistent in a specific synoptic state.

Recent estimations (e.g., Burton-Johnson et al., 2016) suggest that ice-free regions occupy merely 0.18% of the Antarctic continent's land areas, and future projections predict an increase of these areas by up to 25% by the end of the century (Lee et al., 2017). Thus, while the conclusions related to the WAIS Divide may be generally applicable to the Antarctic Plateau regions, the conclusions drawn from McMurdo Station observations may be limited to a small number of ice-free Antarctic sites (at least during large parts of summer), particularly with regard to the CRF. The potentially high impact of frequent (frontal activity) ice clouds on the net surface radiation in coastal regions is most pronounced in SOMs corresponding to a positive SAM index (SOMs 6, 8, and 9), mainly during FRZ and MXSI (see Figure 7), despite the typically lower moisture supply in these seasons (e.g., Carrasco et al., 2003). The positive correlation of the SAM index with cyclonic activity around the Antarctic coasts (e.g., Hosking et al., 2013; Lubin et al., 2008; Uotila et al., 2013; see also the trends in Figure 3) and the long-term incline of the SAM index imply that thick (frontal activity) ice clouds (which are common around the Antarctic coasts, mainly during winter) would have an increasing significant role in the determination of the surface energy budget in the future.

Appendix A: Generating a Cloud Mask Using the MPL Data

After a LDR σ mask with an upper limit fraction of 0.2 is applied on the MPL data, initial classifcation of the MPL returns based on the β_p versus LDR 2-dimensional histogram is performed. However, some uncertainty exists with regard to a large lidar return population (initially classified as "unknown") in a potentially ambiguous region of the histogram (low-LDR with moderate to high β_p). A considerable fraction of this "unknown" population is attributed to the estimated β_p uncertainty and the frequent plate ice-crystal growth regime temperatures during the WAIS Divide deployment. The following steps are implemented to treat the "unknown" population, tune, and correct the phase classification:

1. Convert the entire resolved LBCLs into ice if no LCBH is reported by the MPL LCBH algorithm data product (Silber et al., 2018a, 2018b) within $\pm$100 m and $\pm$15 min from the resolved LBCL base height and occurrence time, respectively. Due to frequent MPL artifacts close to the surface, the ceilometer CBH data are used instead of the MPL LCBH data output up to 200 m AGL, while taking into consideration the typical ~60-m height difference between the two data products (see Silber et al., 2018b).
2. Convert ice grid points above a resolved LBCL into liquid-bearing grid points if the distance from the LBCL top to the detected cloud top is smaller than 100 m (due to the strong attenuation within LBCLs, which significantly influence the MPL parameters).
3. Calculate the MPL 5th and 95th percentiles of the LDR σ, lidar scene variability (the ratio of the lidar copolar signal σ to the copolar noise minus 1), and LDR SNR as a function of height for ice and LBCL grid points. Lower (higher) heights show pronounced differences in scene variability and LDR SNR (LDR σ) between ice and LBCLs, respectively. Smooth the 5th and 95th percentile curves (only at heights where more than 50 samples exist) using a smoothing spline with a smoothing parameter of 10^{-9} (height is taken in meters).
4. Reclassify all the MPL lidar returns based on the β_p versus LDR 2-dimensional histogram.

5. Classify the "unknown" population into liquid-bearing grid points if their LDR σ (scene variability/LDR SNR) is lower (higher) than both the LBCL (ice) 95th and ice (LBCL) 5th percentile smoothed curves at the same level, respectively. Perform the opposite process (look for higher/lower instead of lower/higher values) for classifying the "unknown" into ice grid points.
6. Apply a median filter with a 5 × 5 grid point size and convert all the remaining "unknown" grid points into ice grid points (smooth the cloud mask).
7. Repeat steps 1 and 2.
8. Convert liquid-bearing grid points into ice grid points in LBCLs that are thicker than 400 m (unite overlying layers distant by less than 50 m for the thickness calculation) if their LDR is higher than a fraction value of 0.08 (validate the results).

Appendix B: RRTM Configuration

The RRTM model is run from the surface up to 70 km. Measurements from twice-daily Vaisala MW-31 radiosonde releases at McMurdo Station and four times daily at the WAIS Divide are linearly interpolated in time and height (to fit the cloud mask grid) and used for pressure, temperature, and water vapor model input up to 20 km. A large bin size of 480 m is used in the RRTM SW version to mitigate underflow issues. Smaller grid spacing of 7.5 and 60 m is used in the RRTM LW version up to and above 1 km, respectively. The finer grid at lower levels is utilized to better capture the large low-level atmospheric parameter variability accounting for most of the LW irradiance at the surface (McFarlane et al., 2013; Ohmura, 2001). The lowest bin temperature (designating the surface skin temperature; T_{surf}) is estimated using the graybody approximation:

$$T_{surf} = \left[\frac{LW\uparrow - (1-\varepsilon_{LW})LW\downarrow}{\varepsilon_{LW}\sigma_b}\right]^{0.25}, \tag{A1}$$

where ε_{LW} is the LW emissivity and σ_b is the Stefan-Boltzmann constant. The ε_{LW} value is set to 0.99 for the WAIS, the value of which corresponds to the ε_{LW} of ice (Grenfell et al., 1998; Rees & James, 1992). At McMurdo, the ε_{LW} is estimated based on the variability of the SW absorptivity (A_{SW}; see text below and Figure S3). The minimum and maximum A_{SW} are assumed to correspond with the ε_{LW} of "pure" ice/snow ($\varepsilon_{LW} = 0.99$) and bare volcanic soil ($\varepsilon_{LW} = 0.95$; see Sobrino et al., 2009), respectively. Linear interpolation is used to estimate ε_{LW} corresponding to other A_{SW} values. This ε_{LW} estimation routine is performed only for daytime periods, because of the dependence on the SW measurements ($\varepsilon_{LW} = 0.99$ for all nighttime measurements).

Tests were performed to examine the influence of water vapor variability on short timescales by "normalizing" the sounding profiles based on the ratio between the integrated sounding water vapor to the hourly MWR precipitable water vapor (PWV) retrievals during the release hours. However, these tests did not show a significant influence over the accuracy of the model output; hence, this normalization is omitted from this analysis.

Above 20 km, the default (1-km bin size) sub-Arctic model profiles (McClatchey et al., 1971) are used (the winter profile is utilized between the March and September equinoxes, while the summer profile is used for the rest of the year). Apart from water vapor, six other gas species are incorporated in the model, namely, CO_2, O_3, N_2O, CO, CH_4, and O_2. Monthly CO_2 values from the South Pole Station (Dlugokencky et al., 2017) are used for the entire profile, while the default sub-Arctic model profiles are utilized for the other gases.

The A_{SW} used for the SW flux calculations in daytime periods is estimated on an hourly basis, because of the stark albedo contrast between snow and the volcanic soil on which McMurdo Station is situated, the substantial impact of volcanic dust and melting on the albedo of snow (Warren, 1984), and the dependency of ice surface albedo on the solar zenith angle (Warren, 1982). Daytime periods are defined here as times when the solar zenith angle is smaller than 90°. The hourly A_{SW} used in the RRTM SW model is estimated (using the 1-min resolution data) as one minus the surface albedo, α, given as

$$\alpha = \frac{SW\uparrow}{SW\downarrow}. \tag{A2}$$

Linear interpolation is performed for periods in which data are missing, or when the yielded A_{SW} minus (plus) its hourly σ is smaller (greater) than 0 (1). These false values are predominantly obtained when

either the GNDRAD upwelling or the SKYRAD downwelling SW fluxes are close to the instrument uncertainty level (2% or 10 W/m^2 for GNDRAD and 4% + 2 W/m^2 and 3% for the SKYRAD diffuse and direct components, respectively; see Andreas et al., 2018).

Acknowledgments
AWARE is supported by the DOE ARM Climate Research Facility and NSF Division of Polar Programs. The data used in this study are available in the ARM data archive (http://www.archive.arm.gov). Ten-second resolution HSRL data can be obtained from the University of Wisconsin-Madison HSRL Lidar Group (http://lidar.ssec.wisc.edu). The MPL LCBH data product is available as a PI data product in the ARM data archive (https://www.osti.gov/servlets/purl/1438194). ERA-Interim reanalysis data are accessible via the ECMWF database (https://www.ecmwf.int/en/forecasts/datasets/archive-datasets/reanalysis-datasets/era-interim). Sea-ice extent time series can be viewed and downloaded via the National Snow & Ice Data Center website (https://nsidc.org/data/seaice_index/archives). The data plotted in Figures 5, 6c–6j, 7, and 8 are given in the supporting information. The authors wish to thank Steven Feldstein, Eugene Clothiaux, and Nathaniel Johnson for the fruitful discussions and Lucien Simpfendoerfer for assistance with the RRTM. Chuck Long provided valuable guidance in calculating the downwelling LW radiation. The authors also thank the three anonymous reviewers for their insightful comments and help in improving the manuscript. I. S. and J. V. are supported by the National Science Foundation Grant PLR-1443495 and by the DOE Grant DE-SC0017981. A. M. V. is supported by DOE under contract DE-SC0012704.

References

Andreas, A., Dooraghi, M., Habte, A., Kutchenreiter, M., Reda, I., & Sengupta, M. (2018). Solar Infrared Radiation Station (SIRS), Sky Radiation (SKYRAD), Ground Radiation (GNDRAD), and Broadband Radiometer Station (BRS) instrument handbook. DOE/SC-ARM-TR-025, DOE Office of Science, Office of Biological and Environmental Research. https://doi.org/10.2172/1432706

Bação, F., Lobo, V., & Painho, M. (2005). Self-organizing maps as substitutes for *K*-means clustering. In V. S. Sunderam, G. D. van Albada, P. M. A. Sloot, & J. Dongarra (Eds.), *BT – computational science—ICCS 2005* (pp. 476–483). Berlin, Heidelberg: Springer.

Bennartz, R., Shupe, M. D., Turner, D. D., Walden, V. P., Steffen, K., Cox, C. J., et al. (2013). July 2012 Greenland melt extent enhanced by low-level liquid clouds. *Nature*, *496*(7443), 83–86. https://doi.org/10.1038/nature12002

Brion, J., Chakir, A., Charbonnier, J., Daumont, D., Parisse, C., & Malicet, J. (1998). Absorption spectra measurements for the ozone molecule in the 350–830 nm region. *Journal of Atmospheric Chemistry*, *30*(2), 291–299. https://doi.org/10.1023/A:1006036924364

Bromwich, D. H. (1991). Mesoscale cyclogenesis over the southwestern Ross Sea linked to strong katabatic winds. *Monthly Weather Review*, *119*(7), 1736–1753. https://doi.org/10.1175/1520-0493(1991)119<1736:MCOTSR>2.0.CO;2

Bromwich, D. H., Nicolas, J. P., Hines, K. M., Kay, J. E., Key, E. L., Lazzara, M. A., et al. (2012). Tropospheric clouds in Antarctica. *Reviews of Geophysics*, *50*, RG1004. https://doi.org/10.1029/2011RG000363

Burton-Johnson, A., Black, M., Fretwell, P. T., & Kaluza-Gilbert, J. (2016). An automated methodology for differentiating rock from snow, clouds and sea in Antarctica from Landsat 8 imagery: A new rock outcrop map and area estimation for the entire Antarctic continent. *The Cryosphere*, *10*(4), 1665–1677. https://doi.org/10.5194/tc-10-1665-2016

Cadeddu, M. P. (2010). G-Band Vapor Radiometer Profiler (GVRP) handbook. Doe/SC-Arm/TR-091, Office of Science, DOE Office of Biological and Environmental Research.

Cadeddu, M. P., Payne, V. H., Clough, S. A., Cady-Pereira, K., & Liljegren, J. C. (2007). Effect of the oxygen line-parameter modeling on temperature and humidity retrievals from ground-based microwave radiometers. *IEEE Transactions on Geoscience and Remote Sensing*, *45*(7), 2216–2223. https://doi.org/10.1109/TGRS.2007.894063

Cadeddu, M. P., Turner, D. D., & Liljegren, J. C. (2009). A neural network for real-time retrievals of PWV and LWP from Arctic millimeter-wave ground-based observations. *IEEE Transactions on Geoscience and Remote Sensing*, *47*(7), 1887–1900. https://doi.org/10.1109/TGRS.2009.2013205

Carrasco, J. F., & Bromwich, D. H. (1993). Mesoscale cyclogenesis dynamics over the southwestern Ross Sea, Antarctica. *Journal of Geophysical Research*, *98*(D7), 12,973–12,,995. https://doi.org/10.1029/92JD02821

Carrasco, J. F., Bromwich, D. H., & Monaghan, A. J. (2003). Distribution and characteristics of mesoscale cyclones in the Antarctic: Ross Sea eastward to the Weddell Sea. *Monthly Weather Review*, *131*(2), 289–301. https://doi.org/10.1175/1520-0493(2003)131<0289:DACOMC>2.0.CO;2

Cavalieri, D. J., Parkinson, C. L., Gloersen, P., & Zwally, H. J. (1996). Sea ice concentrations from Nimbus-7 SMMR and DMSP SSM/I-SSMIS Passive Microwave Data, Version 1. https://doi.org/10.5067/8GQ8LZQVL0VL

Cesana, G., Kay, J. E., Chepfer, H., English, J. M., & de Boer, G. (2012). Ubiquitous low-level liquid-containing Arctic clouds: New observations and climate model constraints from CALIPSO-GOCCP. *Geophysical Research Letters*, *39*, L20804. https://doi.org/10.1029/2012GL053385

Chang, C.-H., & Johnson, N. C. (2015). The continuum of wintertime southern hemisphere atmospheric teleconnection patterns. *Journal of Climate*, *28*(24), 9507–9529. https://doi.org/10.1175/JCLI-D-14-00739.1

Coggins, J. H. J., & McDonald, A. J. (2015). The influence of the Amundsen Sea low on the winds in the Ross Sea and surroundings: Insights from a synoptic climatology. *Journal of Geophysical Research: Atmospheres*, *120*, 2167–2189. https://doi.org/10.1002/2014JD022830

Coggins, J. H. J., McDonald, A. J., & Jolly, B. (2014). Synoptic climatology of the Ross Ice Shelf and Ross Sea region of Antarctica: *K*-means clustering and validation. *International Journal of Climatology*, *34*(7), 2330–2348. https://doi.org/10.1002/joc.3842

Cook, D. R. (2018). Surface Energy Balance System (SEBS) handbook. Argonne, IL.

de Boer, G., Eloranta, E. W., & Shupe, M. D. (2009). Arctic mixed-phase stratiform cloud properties from multiple years of surface-based measurements at two high-latitude locations. *Journal of the Atmospheric Sciences*, *66*(9), 2874–2887. https://doi.org/10.1175/2009JAS3029.1

Dee, D. P., Uppala, S. M., Simmons, A. J., Berrisford, P., Poli, P., Kobayashi, S., et al. (2011). The ERA-Interim reanalysis: Configuration and performance of the data assimilation system. *Quarterly Journal of the Royal Meteorological Society*, *137*(656), 553–597. https://doi.org/10.1002/qj.828

Dlugokencky, E. J., Lang, P. ., Mund, J. W., Crotwell, A. M., Crotwell, M. J., & Thoning, K. W. (2017). Atmospheric carbon dioxide dry air mole fractions from the NOAA ESRL Carbon Cycle Cooperative Global Air Sampling Network, 1968–2016, Version: 2017-07-28. Retrieved from ftp://aftp.cmdl.noaa.gov/data/trace_gases/co2/flask/surface/

Eloranta, E. W. (2005). High spectral resolution lidar. In *Lidar: Range-resolved optical remote sensing of the atmosphere* (pp. 143–163). New York, NY: Springer. https://doi.org/10.1007/0-387-25101-4_5

Fielding, M. D., Chiu, J. C., Hogan, R. J., Feingold, G., Eloranta, E., O'Connor, E. J., & Cadeddu, M. P. (2015). Joint retrievals of cloud and drizzle in marine boundary layer clouds using ground-based radar, lidar and zenith radiances. *Atmospheric Measurement Techniques*, *8*(7), 2663–2683. https://doi.org/10.5194/amt-8-2663-2015

Flournoy, M. D., Feldstein, S. B., Lee, S., & Clothiaux, E. E. (2016). Exploring the tropically excited Arctic warming mechanism with station data: Links between tropical convection and Arctic downward infrared radiation. *Journal of the Atmospheric Sciences*, *73*(3), 1143–1158. https://doi.org/10.1175/JAS-D-14-0271.1

Flynn, C. J., Mendozaa, A., Zhengb, Y., & Mathurb, S. (2007). Novel polarization-sensitive micropulse lidar measurement technique. *Optics Express*, *15*(6), 2785–2790. https://doi.org/10.1364/OE.15.002785

Fogt, R. L., Wovrosh, A. J., Langen, R. A., & Simmonds, I. (2012). The characteristic variability and connection to the underlying synoptic activity of the Amundsen-Bellingshausen Seas low. *Journal of Geophysical Research*, *117*, D07111. https://doi.org/10.1029/2011JD017337

Gorodetskaya, I. V., Tsukernik, M., Claes, K., Ralph, M. F., Neff, W. D., & van Lipzig, N. P. M. (2014). The role of atmospheric rivers in anomalous snow accumulation in East Antarctica. *Geophysical Research Letters*, *41*, 6199–6206. https://doi.org/10.1002/2014GL060881

Grenfell, T. C., Barber, D. G., Fung, A. K., Gow, A. J., Jezek, K. C., Knapp, E. J., et al. (1998). Evolution of electromagnetic-signatures of sea ice from initial formation through the establishment of thick first-year ice. *IEEE Transactions on Geoscience and Remote Sensing*, *36*(5), 1642–1654. https://doi.org/10.1109/36.718636

Hartmann, D. L., & Lo, F. (1998). Wave-driven zonal flow vacillation in the Southern Hemisphere. *Journal of the Atmospheric Sciences*, *55*(8), 1303–1315. https://doi.org/10.1175/1520-0469(1998)055<1303:WDZFVI>2.0.CO;2

Hogan, R. J., Mittermaier, M. P., & Illingworth, A. J. (2006). The retrieval of ice water content from radar reflectivity factor and temperature and its use in evaluating a mesoscale model. *Journal of Applied Meteorology and Climatology*, *45*(2), 301–317. https://doi.org/10.1175/JAM2340.1

Hosking, J. S., Orr, A., Marshall, G. J., Turner, J., & Phillips, T. (2013). The influence of the Amundsen–Bellingshausen Seas low on the climate of West Antarctica and its representation in coupled climate model simulations. *Journal of Climate*, *26*(17), 6633–6648. https://doi.org/10.1175/JCLI-D-12-00813.1

Johnson, N. C. (2013). How many ENSO flavors can we distinguish? *Journal of Climate*, *26*(13), 4816–4827. https://doi.org/10.1175/JCLI-D-12-00649.1

Johnson, N. C., Feldstein, S. B., & Tremblay, B. (2008). The continuum of Northern Hemisphere teleconnection patterns and a description of the NAO shift with the use of self-organizing maps. *Journal of Climate*, *21*(23), 6354–6371. https://doi.org/10.1175/2008JCLI2380.1

Jolly, B., Kuma, P., McDonald, A., & Parsons, S. (2018). An analysis of the cloud environment over the Ross Sea and Ross ice shelf using CloudSat/CALIPSO satellite observations: The importance of synoptic forcing. *Atmospheric Chemistry and Physics*, *18*(13), 9723–9739. https://doi.org/10.5194/acp-18-9723-2018

Jones, P. D., New, M., Parker, D. E., Martin, S., & Rigor, I. G. (1999). Surface air temperature and its changes over the past 150 years. *Reviews of Geophysics*, *37*(2), 173–199. https://doi.org/10.1029/1999RG900002

Klein, S. A., McCoy, R. B., Morrison, H., Ackerman, A. S., Avramov, A., Boer, G. ., et al. (2009). Intercomparison of model simulations of mixed-phase clouds observed during the ARM mixed-phase Arctic cloud experiment. I: Single-layer cloud. *Quarterly Journal of the Royal Meteorological Society*, *135*(641), 979–1002. https://doi.org/10.1002/qj.416

Kohonen, T. (1982). Self-organized formation of topologically correct feature maps. *Biological Cybernetics*, *43*(1), 59–69. https://doi.org/10.1007/BF00337288

Kohonen, T. (2013). Essentials of the self-organizing map. *Neural Networks*, *37*, 52–65. https://doi.org/10.1016/j.neunet.2012.09.018

Kushner, P. J., Held, I. M., & Delworth, T. L. (2001). Southern Hemisphere atmospheric circulation response to global warming. *Journal of Climate*, *14*(10), 2238–2249. https://doi.org/10.1175/1520-0442(2001)014<0001:SHACRT>2.0.CO;2

Lee, J. R., Raymond, B., Bracegirdle, T. J., Chadès, I., Fuller, R. A., Shaw, J. D., & Terauds, A. (2017). Climate change drives expansion of Antarctic ice-free habitat. *Nature*, *547*(7661), 49–54. https://doi.org/10.1038/nature22996

Lee, S., & Feldstein, S. B. (2013). Detecting ozone- and greenhouse gas-driven wind trends with observational data. *Science*, *339*(6119), 563–567. https://doi.org/10.1126/science.1225154

Limpasuvan, V., & Hartmann, D. L. (1999). Eddies and the annular modes of climate variability. *Geophysical Research Letters*, *26*(20), 3133–3136. https://doi.org/10.1029/1999GL010478

Lubin, D., Bromwich, D. H., Russell, L. M., Verlinde, J., & Vogelmann, A. M. (2015). ARM West Antarctic Radiation Experiment (AWARE) science plan. Doe/SC-ARM-15-040, DOE Office of Science, Office of Biological and Environmental Research. Retrieved from https://www.osti.gov/servlets/purl/1232663

Lubin, D., Wittenmyer, R. A., Bromwich, D. H., & Marshall, G. J. (2008). Antarctic Peninsula mesoscale cyclone variability and climatic impacts influenced by the SAM. *Geophysical Research Letters*, *35*, L02808. https://doi.org/10.1029/2007GL032170

Mahesh, A., Walden, V. P., & Warren, S. G. (2001). Ground-based infrared remote sensing of cloud properties over the Antarctic plateau. Part II: Cloud optical depths and particle sizes. *Journal of Applied Meteorology*, *40*(7), 1279–1294. https://doi.org/10.1175/1520-0450(2001)040<1279:GBIRSO>2.0.CO;2

Marshall, J. G., Stott, A. P., Turner, J., Connolley, M. W., King, C. J., & Lachlan-Cope, A. T. (2004). Causes of exceptional atmospheric circulation changes in the Southern Hemisphere. *Geophysical Research Letters*, *31*, L14205. https://doi.org/10.1029/2004GL019952

Maslanik, J., & Stroeve, J. (1999). Near-real-time DMSP SSMIS daily polar gridded sea ice concentrations, version 1. https://doi.org/10.5067/U8C09DWVX9LM

Mather, J. H., & Voyles, J. W. (2013). The arm climate research facility: A review of structure and capabilities. *Bulletin of the American Meteorological Society*, *94*(3), 377–392. https://doi.org/10.1175/BAMS-D-11-00218.1

McClatchey, R. A., Fenn, R. W., Selby, J. E. Al, Volz, F. E., & Garing, J. S. (1971). Optical properties of the atmosphere. AFCRL-72-0497, Air Force Cambridge Research Laboratories, Bedford, MA.

McFarlane, S. A., Long, C. N., & Flaherty, J. (2013). A climatology of surface cloud radiative effects at the ARM tropical Western Pacific sites. *Journal of Applied Meteorology and Climatology*, *52*(4), 996–1013. https://doi.org/10.1175/JAMC-D-12-0189.1

Miller, N. B., Shupe, M. D., Cox, C. J., Walden, V. P., Turner, D. D., & Steffen, K. (2015). Cloud radiative forcing at Summit, Greenland. *Journal of Climate*, *28*(15), 6267–6280. https://doi.org/10.1175/JCLI-D-15-0076.1

Mlawer, E. J., Taubman, S. J., Brown, P. D., Iacono, M. J., & Clough, S. A. (1997). Radiative transfer for inhomogeneous atmospheres: RRTM, a validated correlated-k model for the longwave. *Journal of Geophysical Research*, *102*(D14), 16,663–16,682. https://doi.org/10.1029/97JD00237

Monaghan, A. J., Bromwich, D. H., Powers, J. G., & Manning, K. W. (2005). The climate of the McMurdo, Antarctica, region as represented by one year of forecasts from the Antarctic mesoscale prediction system. *Journal of Climate*, *18*(8), 1174–1189. https://doi.org/10.1175/JCLI3336.1

Morris, V. R. (2006). Microwave radiometer (MWR) handbook. ARM-TR-016, DOE Office of Science, Office of Biological and Environmental Research.

Morris, V. R. (2016). Ceilometer instrument handbook. DOE/SC-ARM-TR-020, DOE Office of Science, Office of Biological and Environmental Research.

Morrison, H., de Boer, G., Feingold, G., Harrington, J., Shupe, M. D., & Sulia, K. (2012). Resilience of persistent Arctic mixed-phase clouds. *Nature Geoscience*, *5*(1), 11–17. https://doi.org/10.1038/ngeo1332

Nicolas, J. P., & Bromwich, D. H. (2011). Climate of West Antarctica and influence of marine air intrusions. *Journal of Climate*, *24*(1), 49–67. https://doi.org/10.1175/2010JCLI3522.1

Nicolas, J. P., Vogelmann, A. M., Scott, R. C., Wilson, A. B., Cadeddu, M. P., Bromwich, D. H., et al. (2017). January 2016 extensive summer melt in West Antarctica favoured by strong El Niño. *Nature Communications*, *8*, 15799. https://doi.org/10.1038/ncomms15799

Nigro, M. A., & Cassano, J. J. (2014). Analysis of the Ross Ice Shelf airstream forcing mechanisms using self-organizing maps. *Monthly Weather Review*, *142*(12), 4719–4734. https://doi.org/10.1175/MWR-D-14-00077.1

Ohmura, A. (2001). Physical basis for the temperature-based melt-index method. *Journal of Applied Meteorology*, *40*(4), 753–761. https://doi.org/10.1175/1520-0450(2001)040<0753:PBFTTB>2.0.CO;2

Persson, P. O. G., Fairall, C. W., Andreas, E. L., Guest, P. S., & Perovich, D. K. (2002). Measurements near the Atmospheric Surface Flux Group tower at SHEBA: Near-surface conditions and surface energy budget. *Journal of Geophysical Research*, *107*(C10), 8045. https://doi.org/10.1029/2000JC000705

Pithan, F., Medeiros, B., & Mauritsen, T. (2014). Mixed-phase clouds cause climate model biases in Arctic wintertime temperature inversions. *Climate Dynamics*, *43*(1-2), 289–303. https://doi.org/10.1007/s00382-013-1964-9

Polvani, L. M., Waugh, D. W., Correa, G. J. P., & Son, S.-W. (2010). Stratospheric ozone depletion: The main driver of twentieth-century atmospheric circulation changes in the Southern Hemisphere. *Journal of Climate*, *24*(3), 795–812. https://doi.org/10.1175/2010JCLI3772.1

Raphael, M. N., Marshall, G. J., Turner, J., Fogt, R. L., Schneider, D., Dixon, D. A., et al. (2016). The Amundsen Sea low: Variability, change, and impact on Antarctic climate. *Bulletin of the American Meteorological Society*, *97*(1), 111–121. https://doi.org/10.1175/BAMS-D-14-00018.1

Rees, W. G., & James, S. P. (1992). Angular variation of the infrared emissivity of ice and water surfaces. *International Journal of Remote Sensing*, *13*(15), 2873–2886. https://doi.org/10.1080/01431169208904088

Scott, R. C., & Lubin, D. (2014). Mixed-phase cloud radiative properties over Ross Island, Antarctica: The influence of various synoptic-scale atmospheric circulation regimes. *Journal of Geophysical Research: Atmospheres*, *119*, 6702–6723. https://doi.org/10.1002/2013JD021132

Scott, R. C., & Lubin, D. (2016). Unique manifestations of mixed-phase cloud microphysics over Ross Island and the Ross Ice Shelf, Antarctica. *Geophysical Research Letters*, *43*, 2936–2945. https://doi.org/10.1002/2015GL067246

Scott, R. C., Lubin, D., Vogelmann, A. M., & Kato, S. (2017). West Antarctic ice sheet cloud cover and surface radiation budget from NASA A-Train Satellites. *Journal of Climate*, *30*(16), 6151–6170. https://doi.org/10.1175/JCLI-D-16-0644.1

Sedlar, J., Shupe, M. D., & Tjernström, M. (2012). On the relationship between thermodynamic structure and cloud top, and its climate significance in the Arctic. *Journal of Climate*, *25*(7), 2374–2393. https://doi.org/10.1175/JCLI-D-11-00186.1

Seefeldt, M. W., & Cassano, J. J. (2012). A description of the Ross Ice Shelf air stream (RAS) through the use of self-organizing maps (SOMs). *Journal of Geophysical Research*, *117*, D09112. https://doi.org/10.1029/2011JD016857

Sen Gupta, A., & England, M. H. (2006). Coupled ocean-atmosphere-ice response to variations in the Southern Annular Mode. *Journal of Climate*, *19*(18), 4457–4486. https://doi.org/10.1175/JCLI3843.1

Shupe, M. D. (2011). Clouds at Arctic atmospheric observatories. Part II: Thermodynamic phase characteristics. *Journal of Applied Meteorology and Climatology*, *50*(3), 645–661. https://doi.org/10.1175/2010JAMC2468.1

Shupe, M. D., & Intrieri, J. M. (2004). Cloud radiative forcing of the Arctic surface: The influence of cloud properties, surface albedo, and solar zenith angle. *Journal of Climate*, *17*(3), 616–628. https://doi.org/10.1175/1520-0442(2004)017<0616:CRFOTA>2.0.CO;2

Shupe, M. D., Matrosov, S. Y., & Uttal, T. (2006). Arctic mixed-phase cloud properties derived from surface-based sensors at SHEBA. *Journal of the Atmospheric Sciences*, *63*(2), 697–711. https://doi.org/10.1175/JAS3659.1

Shupe, M. D., Turner, D. D., Walden, V. P., Bennartz, R., Cadeddu, M. P., Castellani, B. B., et al. (2013). High and dry: New observations of tropospheric and cloud properties above the Greenland Ice Sheet. *Bulletin of the American Meteorological Society*, *94*(2), 169–186. https://doi.org/10.1175/BAMS-D-11-00249.1

Shupe, M. D., Walden, V. P., Eloranta, E., Uttal, T., Campbell, J. R., Starkweather, S. M., & Shiobara, M. (2011). Clouds at Arctic atmospheric observatories. Part I: Occurrence and macrophysical properties. *Journal of Applied Meteorology and Climatology*, *50*(3), 626–644. https://doi.org/10.1175/2010JAMC2467.1

Silber, I., Verlinde, J., Eloranta, E. W., & Cadeddu, M. (2018). Antarctic cloud macrophysical, thermodynamic phase, and atmospheric inversion coupling properties at McMurdo Station. Part I: Principal data processing and climatology. *Journal of Geophysical Research: Atmospheres* https://doi.org/10.1029/2018JD028279, *123*, 6099–6121.

Silber, I., Verlinde, J., Eloranta, E. W., Flynn, C. J., & Flynn, D. M. (2018a). HSRL liquid cloud base height/MPL liquid cloud base height. United States. https://doi.org/10.5439/1438194

Silber, I., Verlinde, J., Eloranta, E. W., Flynn, C. J., & Flynn, D. M. (2018b). Polar liquid cloud base detection algorithms for high spectral resolution or micropulse lidar data. *Journal of Geophysical Research: Atmospheres*, *123*, 4310–4322. https://doi.org/10.1029/2017JD027840

Silber, I., Verlinde, J., Eloranta, E. W., Flynn, C. J., & Flynn, D. M. (2018c). Reprocessed MPL data sets. United States. https://doi.org/10.5439/1468777

Simmonds, I., Keay, K., & Lim, E.-P. (2003). Synoptic activity in the seas around Antarctica. *Monthly Weather Review*, *131*(2), 272–288. https://doi.org/10.1175/1520-0493(2003)131<0272:SAITSA>2.0.CO;2

Sinclair, M. R., Renwick, J. A., & Kidson, J. W. (1997). Low-frequency variability of Southern Hemisphere sea level pressure and weather system activity. *Monthly Weather Review*, *125*(10), 2531–2543. https://doi.org/10.1175/1520-0493(1997)125<2531:LFVOSH>2.0.CO;2

Solomon, S., Qin, D., Manning, M., Chen, Z., Marquis, M., Averyt, K. B., Tignor, M., & Miller, H. (Eds) (2007). *Climate change 2007: The physical science basis: Contribution of Working Group I to the Fourth Assessment Report of the Intergovernmental Panel on Climate Change, 2007* (pp. 129–234). Cambridge, UK, and New York: Cambridge University Press.

Sotiropoulou, G., Tjernström, M., Sedlar, J., Achtert, P., Brooks, B. J., Brooks, I. M., et al. (2016). Atmospheric conditions during the Arctic clouds in summer experiment (ACSE): Contrasting open water and sea ice surfaces during melt and freeze-up seasons. *Journal of Climate*, *29*(24), 8721–8744. https://doi.org/10.1175/JCLI-D-16-0211.1

Steinhoff, D. F., Chaudhuri, S., & Bromwich, D. H. (2009). A case study of a Ross ice shelf airstream event: A new perspective. *Monthly Weather Review*, *137*(11), 4030–4046. https://doi.org/10.1175/2009MWR2880.1

Stramler, K., Del Genio, A. D., & Rossow, W. B. (2011). Synoptically driven Arctic winter states. *Journal of Climate*, *24*(6), 1747–1762. https://doi.org/10.1175/2010JCLI3817.1

Town, M. S., Walden, V. P., & Warren, S. G. (2005). Spectral and broadband longwave downwelling radiative fluxes, cloud radiative forcing, and fractional cloud cover over the South Pole. *Journal of Climate*, *18*(20), 4235–4252. https://doi.org/10.1175/JCLI3525.1

Turner, D. D. (2005). Arctic mixed-phase cloud properties from AERI Lidar observations: Algorithm and results from SHEBA. *Journal of Applied Meteorology*, *44*(4), 427–444. https://doi.org/10.1175/JAM2208.1

Turner, D. D. (2007). Improved ground-based liquid water path retrievals using a combined infrared and microwave approach. *Journal of Geophysical Research*, *112*, D15204. https://doi.org/10.1029/2007JD008530

Turner, D. D., Clough, S. A., Liljegren, J. C., Clothiaux, E. E., Cady-Pereira, K. E., & Gaustad, K. L. (2007). Retrieving liquid water path and precipitable water vapor from the Atmospheric Radiation Measurement (ARM) microwave radiometers. *IEEE Transactions on Geoscience and Remote Sensing*, *45*(11), 3680–3690. https://doi.org/10.1109/TGRS.2007.903703

Turner, D. D., Vogelmann, A. M., Austin, R. T., Barnard, J. C., Cady-Pereira, K., Chiu, J. C., et al. (2007). Thin liquid water clouds: Their importance and our challenge. *Bulletin of the American Meteorological Society*, *88*(2), 177–190. https://doi.org/10.1175/BAMS-88-2-177

Uotila, P., Vihma, T., & Tsukernik, M. (2013). Close interactions between the Antarctic cyclone budget and large-scale atmospheric circulation. *Geophysical Research Letters*, *40*, 3237–3241. https://doi.org/10.1002/grl.50560

Warren, S. G. (1982). Optical properties of snow. *Reviews of Geophysics*, *20*(1), 67–89. https://doi.org/10.1029/RG020i001p00067

Warren, S. G. (1984). Impurities in snow: Effects on albedo and snowmelt (review). *Annals of Glaciology*, *5*, 177–179. https://doi.org/10.3189/1984AoG5-1-177-179

Westwater, E. R., Han, Y., Shupe, M. D., & Matrosov, S. Y. (2001). Analysis of integrated cloud liquid and precipitable water vapor retrievals from microwave radiometers during the surface heat budget of the Arctic Ocean project. *Journal of Geophysical Research*, *106*(D23), 32,019–32,030. https://doi.org/10.1029/2000JD000055

Widener, K., Bharadwaj, N., & Johnson, K. (2012). Ka-Band ARM Zenith Radar (KAZR) instrument handbook. United States: PNNL; Richland, WA. https://doi.org/10.2172/1035855

Witze, A. (2016). Antarctic clouds studied for first time in five decades. *Nature*, *529*(7584), 12. https://doi.org/10.1038/529012a

Zuidema, P., Baker, B., Han, Y., Intrieri, J., Key, J., Lawson, P., et al. (2005). An Arctic springtime mixed-phase cloudy boundary layer observed during SHEBA. *Journal of the Atmospheric Sciences*, *62*(1), 160–176. https://doi.org/10.1175/JAS-3368.1